



1 **The climate of the Eastern Mediterranean and the Nile River basin**
2 **2000 years ago using the fully forced COSMO-CLM simulation**

3 Mingyue Zhang¹, Eva Hartmann¹, Sebastian Wagner², Muralidhar Adakudlu³, Niklas Luther³,
4 Christos Zerefos⁴, Elena Xoplaki^{1,3}

5 ¹Climatology, Climate Dynamics and Climate Change, Department of Geography, Justus Liebig University of Giessen,
6 Giessen, 35390, Germany

7 ²Helmholtz-Zentrum Hereon, Geesthacht, 21502, Germany

8 ³Center for International Development and Environmental Research, Justus Liebig University of Giessen, Giessen, 35390,
9 Germany

10 ⁴Research Centre for Atmospheric Physics and Climatology, Academy of Athens, Athens, Greece

11

12 *Correspondence to:* Mingyue Zhang (Mingyue.zhang@geogr.uni-giessen.de)

13 **Abstract**

14 Understanding the past climate at regional scale, the impact of natural variability and sensitivity by studying the
15 underlying dynamics and processes, can provide a point of reference for future climate conditions under anthropogenic
16 forcing. The Eastern Mediterranean (EM) and Nile River basin (NR) regions are of particular interest for the study of past
17 climate due to their location under the influence of major atmospheric teleconnections. We developed a high-resolution
18 regional model for paleoclimate applications, COSMO-CLM, by integrating all external forcings and conducted a
19 transient simulation from 500 BCE to 1850 CE. Principal Component Analysis (PCA) was applied for winter/summer
20 precipitation and temperature to validate the model set up and showed very good agreement between simulated and
21 observational/reanalysis data. Further, 400-362 BCE and 1800-1850 CE have been selected for the comparison of the
22 mean climate conditions of the early Roman period (ERP) and pre-industrial times (PI). The comparison of temperature
23 and precipitation suggests comparable mean climatic conditions with spatial differences in terms of variability within the
24 study regions. Over the Eastern Mediterranean (EM), ERP is wetter and warmer in both winter and summer compared to
25 PI, with higher variability in temperature and precipitation in summer than in winter. In the Nile River basin (NR), ERP
26 summers were wetter and more variable compared to PI. The ERP over NR is warmer by approximately 0.5 °C in winter
27 and cooler by 0.5 °C in summer, with low variability in winter and high variability in summer compared to PI. The
28 relevant large-scale circulation of the two periods shows consistent spatial structures with the corresponding
29 precipitation/temperature EOF patterns, albeit with varying amplitudes. The 2500 years transient simulation sheds light
30 to the paleo climate conditions and relevant atmospheric circulation as well as processes of periods of interest in complex
31 areas with detailed output and comprehensive forcing allowing for better representation of the regional climate variability
32 and change. Comparison of simulated output with proxy records, reconstructions and detailed studies of specific events,
33 e.g., volcanic eruptions, can help to capture the spatiotemporal extent of these events and their impact on climate
34 variability and change, in addition to providing insights into their impact on societal change and human history.

35



36 1 Introduction

37 The global climate undergoes significant changes, characterized by rising temperatures, more intense, more frequent and
38 more persistent extreme weather and climate events and shifting precipitation patterns (Hennessy et al., 2022).
39 Anthropogenic climate change poses a great threat to ecosystems, economies, and human well-being worldwide (Pörtner
40 et al., 2022). The historical context is critical when assessing present-day climate anomalies, attributing them to forcings
41 and making statements regarding their frequency and severity in a long-term perspective (e.g. Luterbacher et al., 2016).
42 Furthermore, the availability of paleoclimatic data spanning centuries to millennia is a vital resource for studying and
43 characterizing climate changes, offering insights that enhance our comprehension of climate variability, trends, extremes,
44 and contributing essential information for climate mitigation and adaptation strategies (Luterbacher et al., 2016;
45 Luterbacher and Pfister, 2015; Haldon et al., 2014, 2018).

46 Studying climate at regional and local scales improves our understanding of the dynamical and physical processes
47 involved. In order to prepare useful climate projections and adequate responses to the impacts of climate change on
48 vulnerable areas (Kelley et al., 2015), a better understanding of the past climate at a high spatial resolution is of great
49 importance. The Eastern Mediterranean (EM) and the Nile River Basin (NR) are located in an area of great climatic and
50 societal interest with a very long history, with important civilizations inhabiting the area for several millennia. Today, the
51 EM area faces substantial societal challenges, partially connected with climate change impacts, including migration and
52 societal disruptions (Lange et al., 2020). The region also represents a prominent climate change hotspot with exceptionally
53 intense warming that exceeds the continental and global averages, while the area experiences an increasing amount of
54 extreme weather events such as heatwaves, droughts, dust storms, heavy precipitation and floods (Zittis et al., 2022).

55 EM is influenced by mid-latitude, subtropical and tropical weather systems (Alpert et al., 2005), which can lead to a range
56 of extremes, including windstorms, hydrological and temperature extremes (Hochman et al., 2022). Situated in a transition
57 zone between subtropical and mid-latitude climates and located at an atmospheric crossroad, the area is directly influenced
58 by a variety of atmospheric circulation patterns and meteorological processes on different continents (Zittis et al., 2022).

59 For example, in the summer the South Asian Monsoon has a major impact on the Eastern Mediterranean, while in winter,
60 the area is affected by the variability of continental circulation anomalies linked to the Siberian High-Pressure System
61 (Cramer et al., 2018; Paz et al., 2003). The extreme weather over EM, such as heavy precipitation, is mainly governed by
62 the large-scale atmospheric circulation and its interaction with regional synoptic systems (i.e., Cyprus Lows, Red Sea
63 Troughs, Persian Troughs, “Sharav” Lows) and high-pressure systems. Complex orographic features further play an
64 important role in the generation of extreme weather (Hochman et al., 2022). Multiple atmospheric circulation patterns
65 affect the NR region and the water availability of the huge drainage basin that crosses different hydroclimatic zones. The
66 precipitation regime along the Nile catchment is mainly related to the West African monsoon, which itself is modulated
67 by the Indian monsoon dynamics (Ménot et al., 2020). Over the central Ethiopian Highlands, the source region of the
68 Blue Nile, 70% of the annual precipitation falls during summer (June-September) when the region is affected by the rain
69 belt of the Intertropical Convergence Zone (ITCZ) and tropical convection clusters over the continental areas (Conway,
70 2000). The climate of the region is also influenced by monsoon systems that prevail around Lake Victoria and sections
71 of the Ethiopian highlands (Camberlin, 2009). The moisture sources that actually affect the NR Basin originate from the
72 Gulf of Guinea, the Indian Ocean and the northern inflow from the Mediterranean Sea and the Red Sea (Viste and
73 Sorteberg, 2013). Most of the wet months in Ethiopia occur in connection with enhanced moisture transport from the
74 north (Viste and Sorteberg, 2013).



75 As in the past, the Nile River is also today the main agricultural and economic water resource for multiple African
76 countries (Singh et al., 2023). Among those, Egypt has always been heavily dependent on the Nile River flow, as one of
77 the Ancient World “*hydraulic civilizations*” (Singh et al., 2023) and thus provides a unique laboratory to study societal
78 vulnerability and response to climate variability (Manning et al., 2017). For example, the Nile floods had significant
79 impacts on the Egyptians’ prosperity, thus various strategies have been made to mitigate, adapt to and take advantage of
80 the impacts of flooding, including technological advancements in water-lifting machines and innovative agricultural
81 practices.

82 The study and better understanding of the climate of the past, its variability, the occurrence of extremes and their
83 interaction with societies are of great significance and scientific interest. It is crucial for gaining insight into current and
84 potential future environmental challenges, and understanding societal and cultural changes (Xoplaki et al., 2016, 2018).
85 The Eastern Mediterranean and northeastern African areas offer a relatively dense network of natural archives and
86 documentary evidence covering the past 2,000 years and indicate the heterogeneous and variable in time and across space
87 climate of the past two millennia (Xoplaki et al., 2016, 2018, 2021; Zittis et al., 2022).

88 The Paleoclimate Modelling Intercomparison Project (PMIP) aims at understanding how the climate system responds to
89 various climate forcings for the documented climate conditions that might differ between historical and current times
90 (Kageyama et al., 2018). At its fourth phase, PMIP4 focuses as well on the comparison between climate reconstructions
91 (based on physical, chemical or biological records) and climate modelling results addressing the ability of state-of-the-art
92 numerical models to realistically simulate climate variability and change of the past, and whether their response to
93 different external forcings is compatible with paleoclimatic evidence (Kageyama et al., 2018). Paleoclimate studies in the
94 Eastern Mediterranean and the Nile Basin mostly rely on proxy records (García-Herrera et al., 2007), climate
95 reconstructions (Luterbacher et al., 2016), and global paleoclimate models with a coarse spatial resolution. The purpose
96 of regional climate models (RCMs) is to refine climate data from coarse-resolution global climate models (GCMs). By
97 doing so, RCMs offer more detailed information at smaller, sub-GCM-grid scales. This increased resolution is particularly
98 valuable for studying regional phenomena and for conducting vulnerability, impacts, and adaptation assessments (Giorgi,
99 2019). Various studies in the field of present-day regional climate modelling (Worku et al., 2018; Alemseged and Tom,
100 2015; Bucchignani et al., 2016) demonstrated that the RCMs outperform their global counterparts in various aspects,
101 mostly related to small-scale meteorological phenomena and the hydrological cycle. Armstrong et al. (2019) found that a
102 regionally limited version of a high spatial resolution atmospheric GCM can simulate more accurately pre-industrial
103 climate and enhance the representation of anomalies in certain past atmospheric processes compared to lower resolution
104 GCMs. By comparing GCM and RCM simulations for different periods in the past, Gomez-Navarro et al. (2012)
105 concluded that their regional model improves the skill to reproduce high-frequency climate patterns over parts of the
106 Mediterranean for the last millennium by better mimicking regional circulation patterns and local climate and hence
107 reducing the biases of the driving GCM. Studies have also highlighted the more realistic representation of topography
108 and the regional climate information that is valuable for paleoclimate studies (Renssen et al., 2001). Considering that the
109 existing proxy and observational data over the study region are geographically restricted over specific parts of the area
110 and the existing GCMs are too coarse, RCMs can help to close this gap by improving the spatial resolution (Bray and von
111 Storch, 2016).

112 Climate variations are also related to changes in external forcing parameters (e.g., orbital, solar, volcanic, land use and
113 greenhouse gases (GHG) (Gómez-Navarro and Zorita, 2013). The climate system is primarily driven by solar radiation,
114 and the variations of solar irradiance can lead to changes at decadal to centennial time scales (Gray et al., 2010). Changes



115 in orbital parameters such as eccentricity, obliquity, and precession also have important effects on the latitudinal and
116 seasonal distribution of solar radiation at different temporal scales (Ludwig et al., 2016; Cubasch et al., 2006). As far as
117 the volcanic forcing is concerned, of the impact of volcanic sulfate aerosols that are injected into the atmosphere by large
118 tropical volcanic eruptions, leads to pronounced stratospheric warming and surface cooling (Robock, 2000; Crowley et
119 al., 2008). Historical studies have matched the Nile flooding with the impact of volcanic eruptions (Manning et al., 2017).
120 Greenhouse gases (GHGs) trap in turn the longwave radiation that is emitted by the Earth surface and lead to a continuous
121 increase of energy in the climate system and effects on the global climate (Ramanathan and Feng, 2009). Furthermore,
122 land use and land cover changes can affect climate by directly altering the surface solar and longwave radiation and
123 indirectly impacting atmospheric turbulence (Pielke Sr et al., 2011; Zhang et al., 2021). When studying palaeoclimate in
124 EM and NR, the climate models used are mainly GCMs, and these forcings are introduced in the GCM simulations. For
125 example, the MPI-ESM-LR which we are using as the input data for the RCM, is fully forced with solar, orbital, volcanic,
126 GHG and land use change (Jungclaus et al., 2017), but those forcings are not yet fully implemented in the RCM, especially
127 for the paleoclimate simulation. Studies have shown that implementing some of the forcings into RCM can have a more
128 accurate representation of regional climate variability (Ludwig et al., 2016, 2017). Hence, the respective changes in
129 external forcings such as solar, orbital, volcanic, GHG and land use change must be implemented into the COSMO-CLM
130 to make the RCM more realistic and consistent with its driving GCM.

131 Thus, we have, to our knowledge, developed the first highly resolved, fully forced, transient paleo regional climate
132 simulation with COSMO-CLM for the period from 500 BCE to 1850 CE. The implementation of the forcings and
133 sensitivity experiments are described in Hartmann et al. (submitted). A temporally and spatially highly resolved, regional
134 simulation across the complete study area (Eastern Mediterranean and Nile River Basin, EMNR) allows the study of
135 regional-to-local paleoclimate processes with higher accuracy. Further, it enables the exploration of the association
136 between the regional climate patterns and the large-scale atmospheric circulation patterns from the GCM world. An asset
137 of the simulation is its contribution to the study of the impact of the occurrence of extreme climate conditions on societies
138 through interdisciplinary, collaborative research.

139 We present and exploit the advantages and breakthroughs of the fully forced, transient simulation by assessing the ability
140 of the simulation to represent the climatic conditions of the area in space and time and the links with the large-scale
141 circulation. The assessment is divided into two approaches, an evaluation during the present time and a comparison of
142 two periods, one in the first millennium BCE and one in the pre-industrial times.

143 The paper is structured as follows: The section "Data and Methods" describes the RCM COSMO-CLM, the reanalysis
144 and observation time series and provides information on the implemented methods. In the section "Results and
145 Discussion", the findings of the analysis are presented and interpreted in detail. Finally, the "Conclusions" section
146 summarizes the main findings and their significance and briefly discusses possible directions for future research.

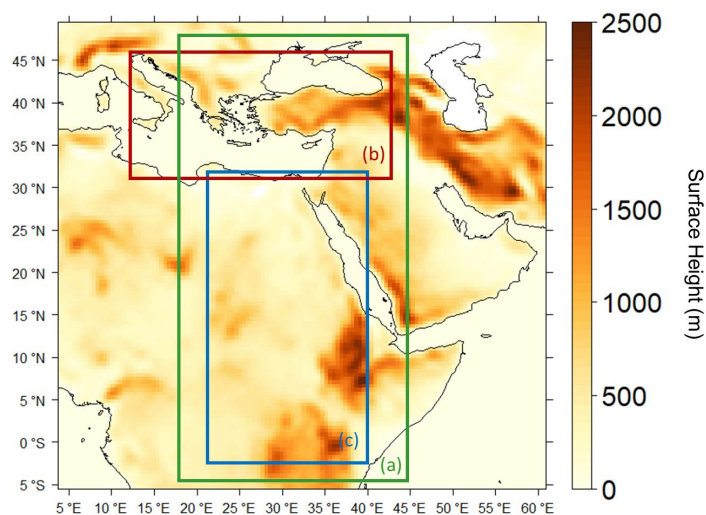
147 **2 Data and methods**

148 **2.1 Regional Climate Model Simulations**

149 The COSMO-CLM (COnsortium for Small-scale MOdelling in CLimate Mode - CCLM) (Rockel et al., 2008) is a widely
150 used RCM that has been used to investigate climate change under different forcings, such as land use, orbital and GHG.
151 The CCLM is originally designed to perform simulations from 1850 CE onward and its performance largely depends on
152 the driving GCM (Armstrong et al., 2019). Multiple CCLM simulations have been recently performed at different



153 resolutions up to very high convection-permitting resolution (Raffa et al., 2023) in the frame of the CORDEX
154 (Coordinated Regional Climate Downscaling EXperiment, <https://cordex.org/>) initiative.
155 In this work, we revolutionize by implementing the CCLM in model version 5.0 with CLM version 16 to an adjusted
156 paleoclimate version, fully forced with orbital, solar, GHG, volcanic and land-use changes (Hartmann et al., submitted).
157 We performed a transient simulation from 500 BCE to 1850 CE at the Deutsches Klimarechenzentrum (DKRZ), which
158 is forced with the new MPI-ESM-LR simulation “Mythos” that is performed under the CMIP6 protocol after 1 AD (MPI-
159 ESM-LR ‘past2k’) (Jungclaus et al., 2017) at $\sim 1.875^\circ$ resolution. The period 500 BCE until 1 BC is according to the
160 external forcings used by Bader et al., (2020) in a simulation for the entire Holocene.
161 The implemented forcings in COSMO-CCLM are identical to those of MPI-ESM-P “Mythos” simulation, namely, the
162 orbital forcing is represented by the eccentricity, the obliquity and the longitude of perihelion (Berger, 1978) and the solar
163 forcing by the total solar irradiance (Jungclaus et al., 2017). The changes in GHG concentrations consist of CO₂, CH₄ and
164 N₂O (Meinshausen et al., 2017), while the volcanic forcing is based on the stratospheric aerosol optical depth (AOD) at
165 550 nm wavelength by Toohey and Sigl, (2017).
166 The interpolation of the driving data to the model is done with INT2LM in version 2.05 with CLM version 1
167 (INT2LM-v2.05clm1) (Schättler and Blahak, 2017). The time integration is the two-step Runge-Kutta scheme (Jameson
168 et al., 1981) with a 300 seconds time step. The convection parameterization based on the Tiedtke scheme (Tiedtke, 1988)
169 is used. The representation of albedo and aerosols are found to be the most important parameters in the studied region
170 (see also Hartmann et al., submitted) and are set the same as in Bucchignani et al., (2016). The land surface model is
171 TERRA-ML (Doms et al., 2011; Schulz et al., 2016). The simulations are carried out in a domain including the Eastern
172 Mediterranean, the Middle East and the Nile River Basin from Lake Victoria to the Nile Delta (Fig. 1, 4° – 60° E, 5° S –
173 49° N). For the analysis of the precipitation, we consider the areas of the Eastern Mediterranean (EM, Fig 1b) and the
174 Nile River Basin (NR, Fig. 1c) separately as the precipitation regimes are significantly different between the two regions.
175 While for the analysis of temperature, we have selected a region, include the Eastern Mediterranean and Nile River basin
176 (EMNR, Fig. 1a).
177 The following periods have been used for the assessment of the fully forced, transient CCLM simulation: i) present period
178 (1980-2018) to validate the adjusted COSMO-CLM, ii) the pre-industrial period (PI; 1800-1850 CE), and iii) the Early
179 Roman Period (ERP; 400-362 BCE) for the comparison of the mean climate conditions of the two periods and changes
180 in the climate characteristics of the study region.



181
182 **Figure 1: Topography of the study regions (a) EMNR: indicated with green rectangle, (b) EM: indicated with red rectangle, (c)**
183 **NR: indicated with blue rectangle. Area (a) is used for the analysis of temperature and the other two areas (b, c) are used for**
184 **the analysis of precipitation.**

185 2.2 Observational Time Series and Reanalysis Data

186 We validate the CCLM output, with different observational and reanalysis data sets at 0.5° resolution for the present
187 period, 1980-2018: the monthly mean temperature and total precipitation from CRU TS v.4.05 (Harris et al., 2020), the
188 precipitation climatology from the Global Precipitation Climatology Centre V.2020 (GPCC) (Schneider et al., 2022); and
189 finally the ERA-Interim temperature (Dee et al., 2011) as an additional comparison data set. We restrain from using the
190 ERA-Interim precipitation due to its dependence on GPCC observations. The CRU TS is the reference data set of the
191 validation of the present CCLM simulation output.

192 2.3 Methods

193 2.3.1 Principal Component Analysis

194 Principal Component Analysis (PCA), also referred to as empirical orthogonal functions (EOFs), is a frequently applied
195 technique in climate sciences and multivariate datasets to reduce the dimensions of the dataset and find a smaller number
196 of independent variables conveying as much of the original information (w.r.t. to the variance) as possible (Wilks, 2011).
197 The technique enables the investigation of spatial variability modes by detecting structures in the data (Gallacher et al.,
198 2017; Bader et al., 2020).

199 Eq. (1) shows the covariance matrix C_{XX} (where XX represents the detrended seasonal anomalies of temperature and
200 precipitation) is decomposed according to

$$201 C_{XX} \cdot e = \lambda \cdot e \quad (1)$$

202 This decomposition includes a restructuring of the covariance matrix C_{XX} with the most important patterns (eigenvectors,
203 e) and their principal components (PCs) showing the highest amount of spatial variance (represented by the eigenvalue λ)
204 within the full fields. The classic patterns, EOFs, are orthogonal, hence, the eigenvectors are uncorrelated. For some
205 applications, this is a useful characteristic (i.e., setting up multiple regression models with predictors that are not



206 collinear). In meteorological applications, however, the orthogonality constraint may be disadvantageous, because most
207 processes in the real world are not orthogonal (Storch and Zwiers, 1984). We thus applied the VARIMAX rotation to
208 obtain rotated EOFs (re_j , REOFs) that are physically more consistent than the non-rotated patterns. REOFs are thus used
209 for the validation of the model set-up in the present period (1980 - 2018 CE), while non-rotated EOFs are implemented
210 for the comparison of the mean climate conditions in PI and ERP times.

211 The PCs provide the temporal evolution of the (rotated) eigenvectors re_j and are calculated by projecting the original
212 seasonal anomaly precipitation and temperature time series X onto the (rotated) eigenvectors re_j (REOFs), see Eq. (2):

$$213 \quad PC_j = \langle X | re_j \rangle \quad (2)$$

214 where $\langle | \rangle$ denotes the dot product and j the index of the according principal component and rotated eigenvector,
215 respectively.

216 2.3.2 Validation of the Model Set-up (1980-2018)

217 For the comparison between observed/reanalysis and simulated temperature and precipitation in the present time (1980-
218 2018), we want to compare spatially homogeneous climatic regions in the study area of the simulated and observed
219 datasets. For this purpose, spatial correlations between the first six REOFs of the reference dataset CRU and all REOFs
220 of CCLM and GPCC are calculated to identify the best matching patterns among them. A two-sided t-test was conducted
221 to address the correlations' significance. The retained first six CRU REOFs account for around 75% of the total explained
222 variance in each season and eventually in each data set. For the regions definition, the 80th (75th) percentile of the
223 precipitation (temperature) REOF loadings is calculated. For the "paired" REOFs, six regions are defined by those grid
224 points that exceed the 80th (75th) percentiles of precipitation (temperature). Precipitation and temperature differences are
225 then calculated with respect to the reference CRU data set for the period 1980-2018 and each region. Taylor diagrams
226 containing the Pearson correlation coefficient, the root-mean-square error (RMSE) error, and the standard deviation
227 against the reference data CRU are then prepared for each region for the validation and skill assessment of the COSMO-
228 CLM simulations.

229 2.3.3 Mean Climate Conditions: Pre-industrial and first millennium BCE

230 The mean climate conditions between the first millennium BCE and the pre-industrial times are investigated by addressing
231 differences in mean values and standard deviations together with their statistical significance with a student's t-test at
232 each grid point at the 95% confidence level. By examining temperature variations during these periods, we gain valuable
233 insight into differences at the beginning and end of the simulation period. In order to investigate the relevant atmospheric
234 circulation in the two periods, the non-rotated temperature and precipitation PCs were linearly regressed onto the global
235 sea level pressure (SLP) anomalies from the MPI-ESM-P simulation "Mythos" to estimate the local regression
236 coefficients for the SLP field, see Eq. (3):

$$237 \quad PC(j) = \beta_0(j, k) + \beta_1(j, k) * SLP(k) + \varepsilon(j, k) \quad (3)$$

238 The index k represents the grid-point index covering the geographical domain. $PC(j)$ is the j th non-rotated principal
239 component and $\beta_1(j, k)$ presents the regression coefficients for the j th component on grid point k , and $SLP(k)$ is the SLP
240 time series of grid point k . $\beta_0(j, k)$ is the intercept of the regression and $\varepsilon(j, k)$ as the noise component of grid point k
241 for the j th non-rotated principal component. In our case $j = 1, 2, 3$, i.e., the leading three non-rotated PCs. Please note
242 that in this study, only the regression coefficients $\beta_1(j, k)$ are used to plot the regression map.



243 **3 Results and Discussion**

244 **3.1 Evaluation of the CCLM output**

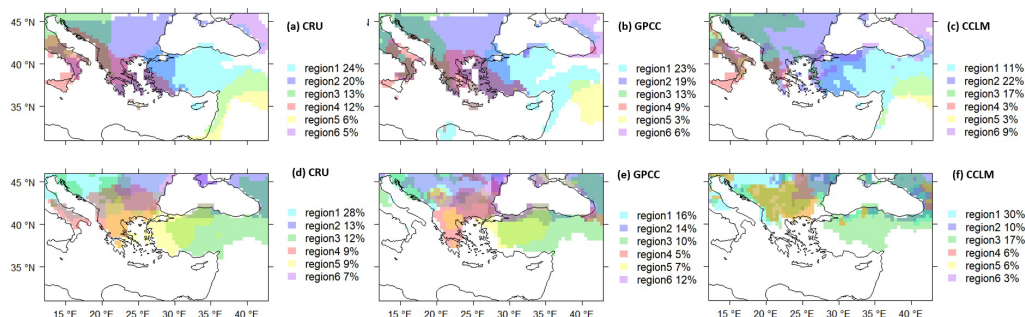
245 **3.1.1 Precipitation – EM**

246 The spatial correlations between the seasonal CRU, CCLM and GPCP REOFs for the period 1980-2018 are presented in
 247 Table 1. The two-sided t-test at the 95% confidence level showed that all correlations are significant. CRU and CCLM
 248 REOFs seem to agree well with the highest significant correlation of 0.94 for winter (DJF) and summer (JJA). Lower
 249 correlations, however, characterize mainly REOFs of lower explained variance.

250 **Table 1: Spatial correlation of the CCLM with CRU and GPCP precipitation REOFs for winter (DJF) and summer (JJA) over**
 251 **the EM. All values are significant at the 95% significance level. Numbers in parentheses give the corresponding REOFs of each**
 252 **data set.**

Winter (December to February)						
$r_{\text{CRU-CCLM}}$	0.70 (1 & 4)	0.85 (2 & 1)	0.91 (3 & 2)	0.74 (4 & 8)	0.74 (5 & 7)	0.88 (6 & 5)
$r_{\text{GPCP-CCLM}}$	0.62 (1 & 4)	0.83 (2 & 1)	0.92 (3 & 2)	0.66 (4 & 6)	0.85 (5 & 5)	0.65 (6 & 4)
Summer (June to August)						
$r_{\text{CRU-CCLM}}$	0.94 (1 & 1)	0.86 (2 & 3)	0.67 (3 & 2)	0.67 (4 & 5)	0.40 (5 & 5)	0.74 (6 & 11)
$r_{\text{GPCP-CCLM}}$	0.92 (1 & 1)	0.79 (2 & 3)	0.69 (3 & 11)	0.71 (4 & 4)	0.60 (5 & 2)	0.33 (6 & 2)

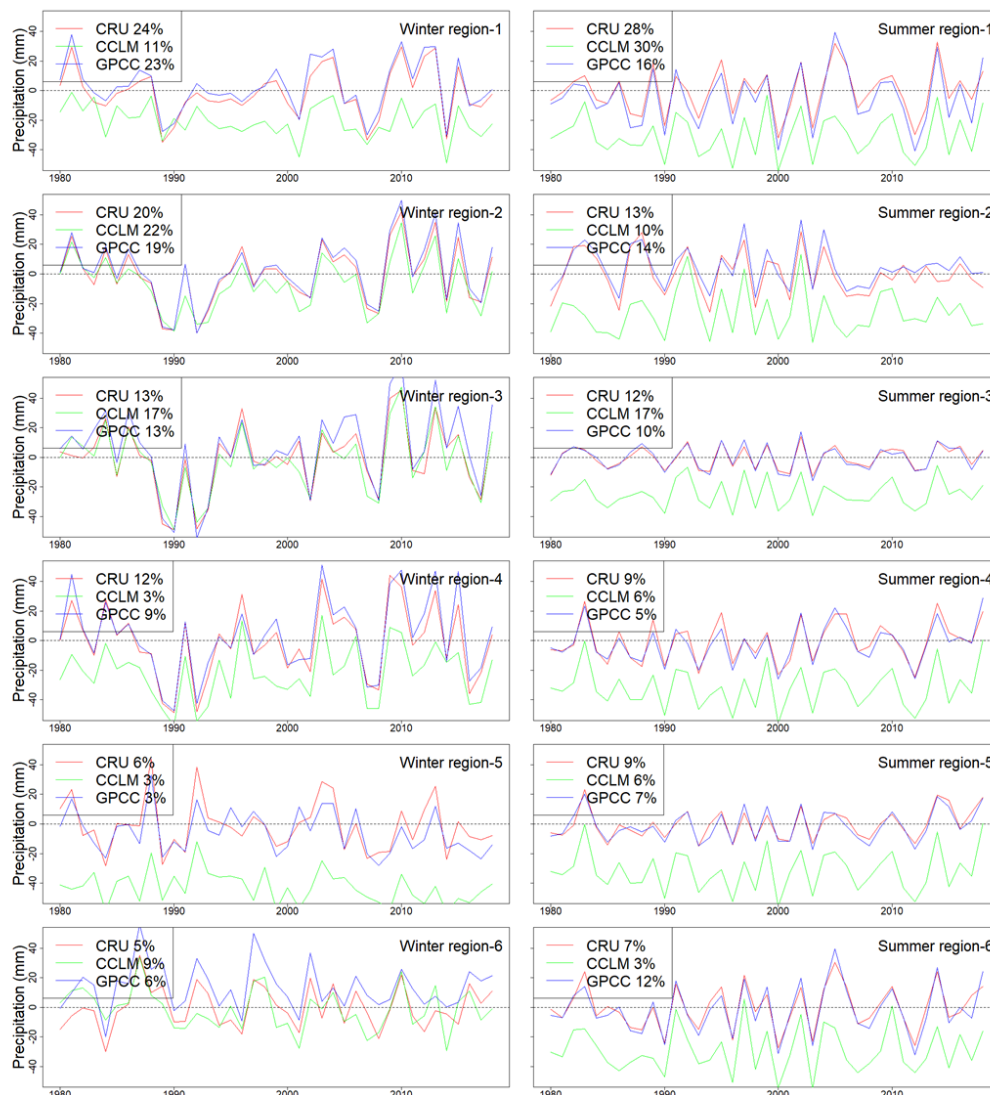
253
 254 The derived winter and summer precipitation regions are shown in Figure 2. Each map is based on the paired REOFs of
 255 each data set with CRU, as shown in Table 1, and the regions are numbered according to the CRU REOFs ranking. For
 256 example, GPCP winter region 5 corresponds to GPCP REOF11 as the counterpart to CRU REOF5. The explained
 257 variance of each REOF is presented along the regions. The three precipitation data sets show a stronger agreement during
 258 winter over the EM. Some regions show a very good agreement between the data sets, such as the winter precipitation
 259 region 2 of CCLM (REOF1) and CRU (REOF2) over the Balkans. Other areas, such as the CCLM region 4 in winter do
 260 not agree well with CRU and GPCP, and the CCLM regions agree less well in the summer with both CRU and GPCP,
 261 especially along the Aegean Sea and the Black Sea coasts. In general, summer precipitation over the EM is mostly
 262 convective and thus very local, leading to a lack of agreement between the observational data sets and the simulation. The
 263 strong bias shown in Figure 3 might be due to an underestimation of its strength and cloud cover (Bucchignani et al.,
 264 2016).



265
 266 **Figure 2: Regionalization of precipitation over the EM in winter (DJF, upper panel) and summer (JJA, lower panel) for CRU**
 267 **(a, d), GPCP (b, e) and CCLM (c, f). The total explained variance of the corresponding REOF is shown in the legend.**



268 The mean regional total precipitation differences of the six regions for GPCC and CCLM with respect to the 1980-2018
 269 mean total CRU winter and summer precipitation are shown in Figure 3. The simulated seasonal variability of
 270 precipitation agrees well with the two observational data sets, although the systematic underestimation of CCLM in
 271 summer is noticeable. Very good agreement is visible for winter precipitation in regions 2 and 3 around the west and
 272 south coast of the Black Sea area. The simulated mean total precipitation differences with respect to CRU for the six
 273 regions show a correlation higher than 0.7 and comparable standard deviation for both seasons and data sets, implying
 274 that the CCLM is performing well in representing the precipitation variability in the EM region (see Figure B1).



275
 276 **Figure 3: Seasonal mean total precipitation differences of EM regions with respect to the 1980-2018 mean total CRU winter**
 277 **(DJF) and summer (JJA) precipitation.**



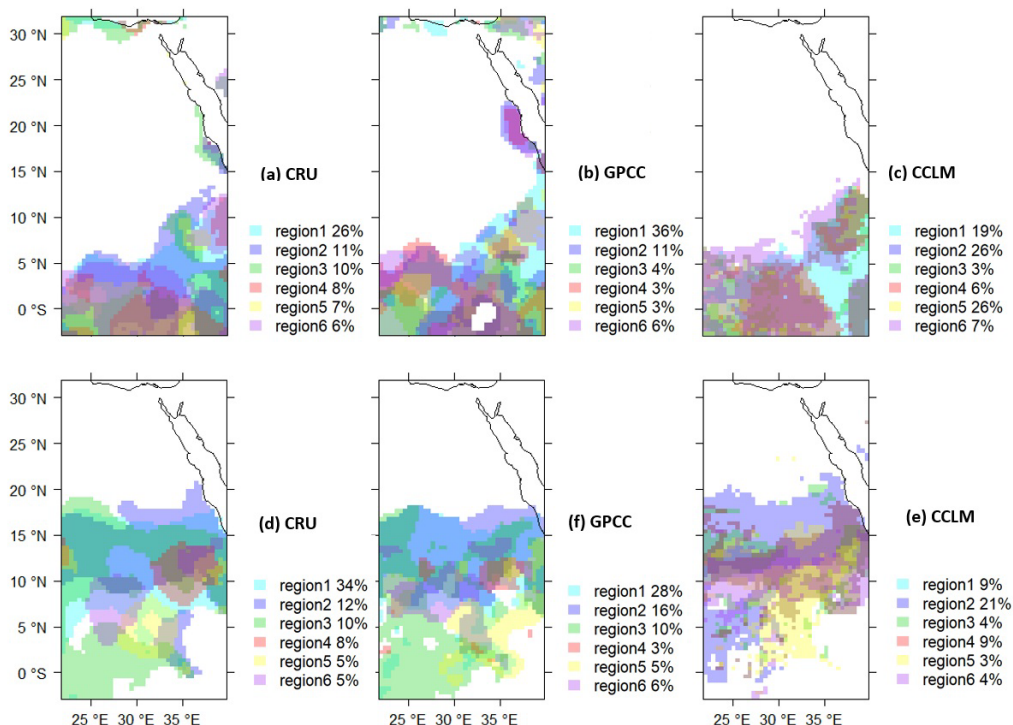
278 **3.1.2 Precipitation – NR**

279 The EM and NR are characterized by significantly different precipitation regimes, and we have thus separated the two
 280 areas for the analysis. The spatial correlation among the REOFs of the three data sets is calculated to determine the
 281 associated regions with respect to CRU, as presented in Table 2. The correlation of REOFs for precipitation in NR is for
 282 some pairs significantly lower compared to the correlations of EM. The CCLM does not perform as well in simulating
 283 precipitation over NR, which may be related to the effect of the Hadley circulation, strong convection in the ITCZ
 284 combined with subtropical advection of hot, dry air linked with the near-surface trade winds (Adam et al., 2016). The
 285 poorer performance of CCLM over the African region may further be connected to an inaccurate representation of cloud
 286 coverage, particularly along the ITCZ (Sørland et al., 2021). Finally, the NR station time series that enter the gridded
 287 CRU and GPCP data sets are sparse, which may also reduce their quality (Harris et al., 2020; Schneider et al., 2022).

288 **Table 2: Spatial correlation of the CCLM with CRU and GPCP precipitation REOFs for winter (DJF) and summer (JJA) over**
 289 **the NR. All values are statistically significant at the 95% significance level. Numbers in parentheses give the corresponding**
 290 **REOFs of each data set.**

Winter (December, January, February)						
$r_{\text{CRU-CCLM}}$	0.79 (1 & 2)	0.71 (2 & 1)	0.29 (3 & 9)	0.50 (4 & 5)	0.74 (5 & 1)	0.50 (6 & 4)
$r_{\text{GPCP-CCLM}}$	0.77 (1 & 2)	0.77 (2 & 1)	0.60 (3 & 3)	0.62 (4 & 5)	0.52 (5 & 6)	0.21 (6 & 4)
Summer (June, July, August)						
$r_{\text{CRU-CCLM}}$	0.64 (1 & 4)	0.56 (2 & 1)	0.37 (3 & 8)	0.63 (4 & 4)	0.40 (5 & 13)	0.26 (6 & 7)
$r_{\text{GPCP-CCLM}}$	0.55 (1 & 4)	0.60 (2 & 4)	0.48 (3 & 5)	0.32 (4 & 13)	0.18 (5 & 8)	0.41 (6 & 3)

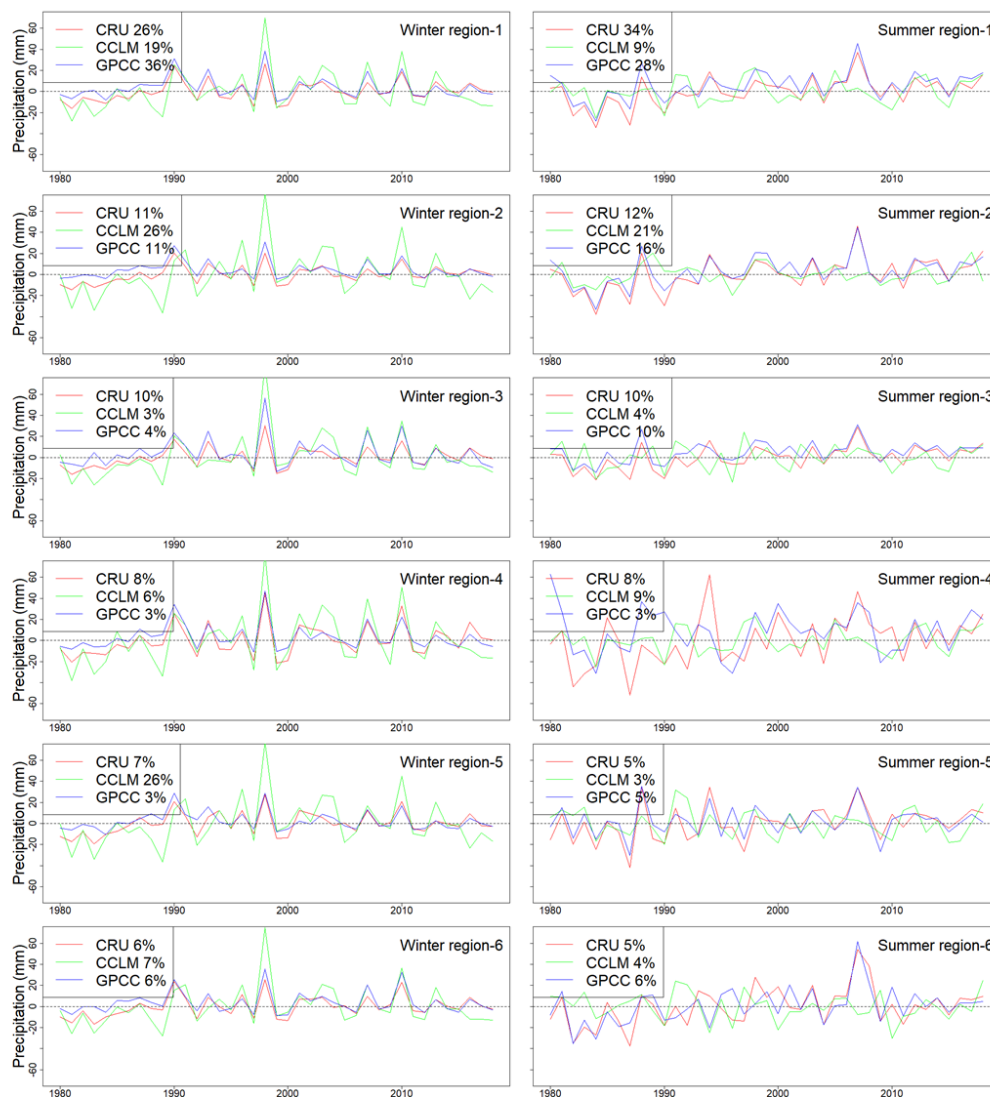
291
 292 Figure 4 shows the corresponding regions based on the REOFs for each of the three data sets (CRU, GPCP, and CCLM),
 293 the explained variance of each REOFs is shown for each region. Precipitation in NR is mainly concentrated in the southern
 294 part of the area, and south of the Sahara desert. In addition, the regions of CCLM over NR exhibit a less homogeneous
 295 pattern compared to the other two data sets. This may be also related to the parameterization of CCLM which is better
 296 optimized for Europe than other areas, especially compared to complex and completely different geographical regions
 297 such as NR (Sørland et al., 2021). In the summer, the regions shift farther north compared to winter, which is related to
 298 rainfall variability due to the seasonal shift of the ITCZ (Nicholson, 2018) and the monsoon rain band (Dieng et al., 2016).
 299 The explained variance varies more between winter and summer compared to EM. For instance, the selected six leading
 300 REOFs of CCLM explain 70 % of the variance in winter but only 50 % in summer.



301

302 **Figure 4: Regionalization of precipitation over the NR in winter (DJF, upper panel) and summer (JJA, lower panel) for CRU**
 303 **(a, d), GPCC (b, e) and CCLM (c, f). The total explained variance of the corresponding REOF is shown in the legend.**

304 The seasonal precipitation differences, with respect to CRU (1980-2018), are presented for the six identified regions of
 305 NR (Fig. 5). Differences between the simulated and observed winter precipitation are smaller than those for EM, and all
 306 wet and dry extremes are overestimated by CCLM. In summer, there is a lack of agreement between the simulated and
 307 observed precipitation, in most cases, while the two observational data sets fail to agree as well. This is visible in the low
 308 correlations between the simulated and observational REOFs. As for the EM region, the Taylor Diagram illustrates the
 309 correlation and standard deviation of the seasonal mean total precipitation differences across the six regions in NR (Fig.
 310 B2). Compared to the EM region, the simulated precipitation in NR exhibits larger biases in terms of standard deviation
 311 compared to CRU (Fig. B2).



312
 313
 314

Figure 5: Seasonal mean total precipitation differences of NR regions with respect to the 1980-2018 mean total CRU winter (DJF) and summer (JJA) precipitation.

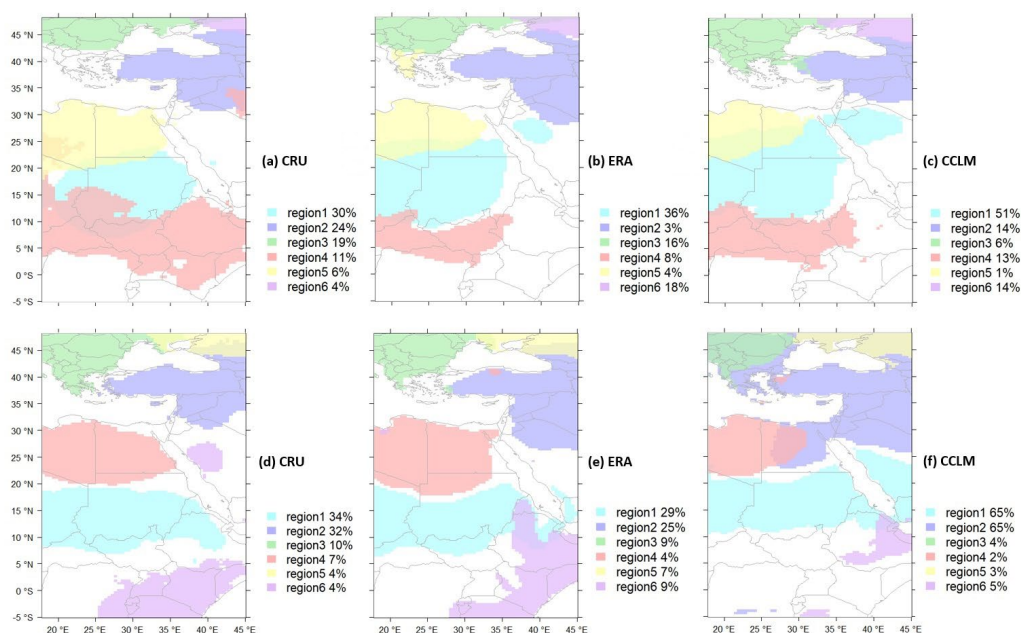
315 **3.1.3 Temperature - EMNR**

316 The temperature analysis encompasses the Eastern Mediterranean and Nile River Basin (EMNR). In Table A1 are
 317 presented the correlation coefficients between the three datasets REOFs (CRU-CCLM, CRU-ERA). The simulated
 318 temperature is highly correlated with both CRU and ERA-Interim data in winter and in summer, supporting the good
 319 performance of the RCM for this variable.

320 Figure 6 shows the regions based on the temperature REOFs of the three data sets and the explained variance of the
 321 REOFs for each region. The regions have a good agreement in space, which indicates as well the good agreement of the
 322 temperature variance of each region. Overall, the regions in all three data sets are spatially coherent regardless of the



323 season. The mean regional temperature differences of the six regions for GPCC and CCLM with respect to the 1980-2018
 324 mean total CRU winter (DJF) and mean summer (JJA) temperature are shown in Figure B3. A clear agreement between
 325 the interannual variability of the CCLM simulations and the observations/reanalysis is observed, however, differences are
 326 found mainly in the maximum and minimum temperatures for specific regions and seasons. In region 1, CCLM
 327 underestimates temperature both in winter and summer. Similarly, the simulated temperature is clearly lower in region 5
 328 during winter and higher in region 6 during summer compared to the observational data sets. Such deviations from
 329 observations in the simulated temperature may be connected with differences in simulated cloud cover and other variables
 330 in the equatorial area affected by the ITCZ (Sørland et al., 2021).
 331 An overall strong correlation between the CCLM seasonal mean temperature and the observational/reanalysis data sets is
 332 further illustrated in the Taylor diagrams (Fig. B4). The over/underestimation of temperature in specific regions is
 333 observed in Figure B3, and those regions also show lower correlation to CRU data (Fig. B4). During winter, a better
 334 agreement is observed between simulated and observational temperatures compared to summer.



335
 336 **Figure 6: Regionalization of temperature over the EMNR in winter (DJF, upper panel) and summer (JJA, lower panel) for**
 337 **CRU (a, d), GPCP (b, e) and CCLM (c, f). The total explained variance of the corresponding REOF is shown in the legend.**

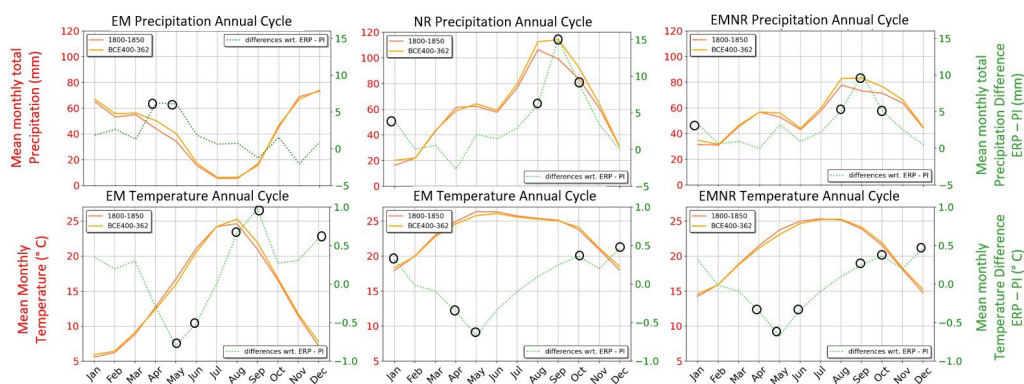
338 3.2 Early Roman Period and Pre-Industrial climates: similarities and differences

339 In this section, we analyze the CCLM simulation for two periods in the past, namely the PI (1800-1850 CE) and ERP
 340 (400-362 BCE) periods. The selection of the two periods is based on two reasons: Firstly, both periods experienced a
 341 series of volcanic eruptions as reflected in the reconstructions by Toohy and Sigl, (2017), and secondly, the two periods
 342 represent the earliest and latest periods of our transient simulation (from 500 BCE to 1850 CE).

343 Figure 7 presents the precipitation and temperature annual cycle of the three regions (EM, NR and EMNR) and the
 344 selected two periods. The absolute monthly mean total precipitation and monthly mean temperature are displayed on the
 345 left y-axis, while the right y-axis represents the differences between the ERP and PI of each month for precipitation and



346 temperature, respectively. Similar mean climate conditions characterize the two periods over the study area. The
 347 precipitation and temperature annual cycles of the two periods are similar, with slight differences for precipitation in the
 348 NR, also reflected in EMNR. In the EM region, the largest differences in monthly precipitation of approximately 5 mm
 349 occur in April and in May, whereas in the NR region, the most notable differences of 15 mm occur in September. The
 350 ERP temperatures are approximately 1 °C warmer in September compared to the PI period in the EM and up to 1 °C
 351 cooler in May over the three study areas. Similar findings were obtained when comparing CCLM simulations with and
 352 without orbital forcing. The orbital forcing leads to increased autumn temperatures while causing a decrease in winter
 353 and spring temperatures (Hartmann et al., submitted). Nevertheless, it is important to note that Figure 7 represents the
 354 spatial mean of each region, and therefore, spatial variations may be averaged out.



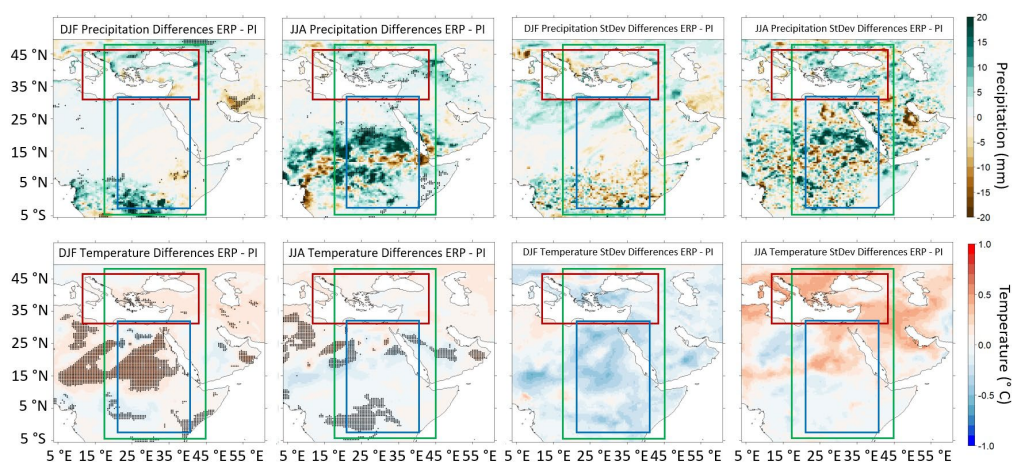
355
 356 **Figure 7: Precipitation and temperature annual cycle of the PI and ERP periods for EM, NR and EMNR. Monthly mean total**
 357 **precipitation and monthly mean temperature are presented on the left y-axis. Differences between ERP and PI (ERP minus**
 358 **PI) are shown on the right y-axis. Significant differences at a 95% confidence level according to a two-sided student t-test are**
 359 **marked with a black circle.**

360 To explore the spatial differences between the two selected periods (ERP and PI) and the three regions (EM, NR, EMNR),
 361 we calculated the mean and standard deviation differences (ERP minus PI) for precipitation and temperature, shown in
 362 Figure 8. The dotted areas indicate statistically significant differences assessed with a t-test at the 95% confidence level.
 363 There are notable differences in precipitation over the EM region (Fig. 8, upper panel, red rectangle), in both winter and
 364 summer. Compared to the PI period, the ERP winters experienced lower precipitation along the northern and eastern
 365 coasts of the Eastern Mediterranean Sea, and increased rainfall over the Balkans and the southern coast of the Black Sea.
 366 In addition, the ERP winter season shows less variability over the entire Greek peninsula and more variability over the
 367 northern Balkans and southern Black Sea. Summers during the ERP period are relatively wetter across the entire EM
 368 region compared to the PI period, with statistically significant differences in some parts of the Balkans. The variability is
 369 higher in most parts of the EM region during the ERP summer period, except the eastern coast of the Black Sea. However,
 370 in both winter and summer, the mean differences are not statistically significant at the 95% level over most of the EM
 371 area.

372 The blue rectangles in the upper panel of Figure 8 show the precipitation differences between the two study periods for
 373 the NR region. During the winter, most of the NR region experienced drier conditions during the ERP compared to the
 374 PI. However, significantly wetter winters (about 20 mm) are found for the southwestern part of the NR region. In summer,
 375 the difference in rainfall between the two periods is more pronounced in the NR compared to the EM, with more areas
 376 experiencing statistically significant wetter conditions during the ERP than in the PI, and drier conditions over Southern
 377 Sudan and the Ethiopian Highlands. It is noteworthy that the standard deviation in the summer shows considerable



378 differences across the NR region reflecting the underlying hydrological conditions and local-scale tropical convective
379 activity.
380 The lower panel of Figure 8 shows the temperature differences for the three regions (EM, NR, EMNR). Accordingly, the
381 ERP winters are warmer compared to the PI period, particularly over the EM and the northern parts of NR. Among the
382 three studied regions, the difference in summer temperatures between the two periods is relatively small, within 0.5 °C.
383 On the other hand, the standard deviation of temperature during the two periods shows distinct differences between
384 summer and winter. The ERP winter temperature is overall less variable compared to the PI period, whereas the ERP
385 summers show higher temperature variance (around 0.7 °C), especially over the EM region and the northern NR region
386 compared to PI.



387
388 **Figure 8: Seasonal differences (ERP minus PI) for winter (DJF) and summer (JJA) mean and standard deviation (StDev) of**
389 **total precipitation over EM (red rectangle), NR (blue rectangle) and 2m air temperature over EMNR (green rectangle). Dotted**
390 **areas indicate statistical significance at the 95% confidence level according to the local student's t-test.**

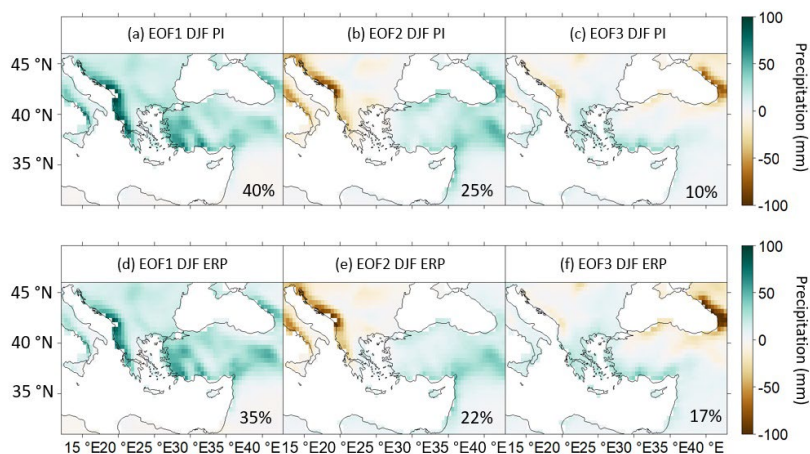
391 3.3 Connection to atmospheric circulation

392 To establish the link between the large-scale atmospheric circulation and local climate in the ERP and PI periods, we
393 explore in this section the connections between SLP and seasonal precipitation and temperature. We present results for
394 winter precipitation over EM and summer temperature over EMNR and we restrict from using the precipitation data over
395 the NR region part due to the limitations of CCLM to accurately simulate precipitation over the area. By examining the
396 leading non-rotated EOFs, we gain insight into the dominant patterns of variability in winter precipitation and summer
397 temperature within these two regions.

398 Figure 9 displays the three leading EOF patterns for the PI (a, b, c) and ERP (d, e, f) periods with the corresponding
399 explained variance. For both periods, they show similar patterns with 75% cumulative total explained variance. EOF1
400 resembles the mean winter precipitation spatial distribution with highest precipitation anomalies along the western coasts
401 of the peninsulas, indicating the influence of the westerly circulation and the land-sea interaction. The second EOF
402 displays a dipole pattern with negative precipitation anomalies over the western and positive precipitation anomalies over
403 the eastern part of EM, likely connected with the direct impact of the large-scale circulation. The higher index EOF3 is
404 characterized by a weaker dipole with distinct lower precipitation along the eastern coasts of the Black Sea and higher



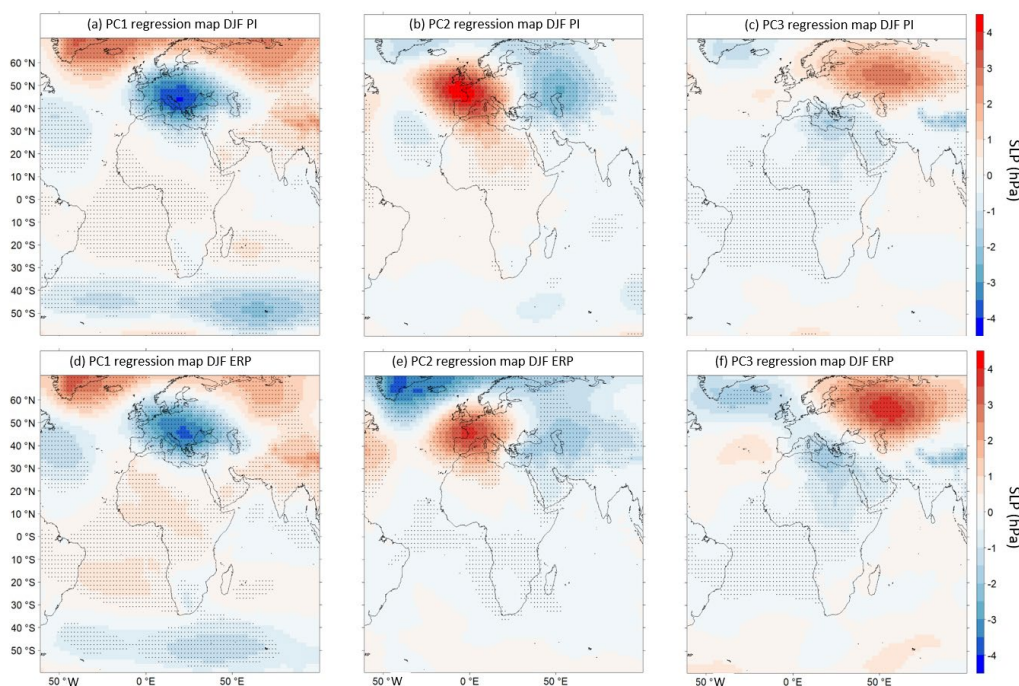
405 precipitation in the southern Mediterranean coastal areas. Smaller differences are observed in the total explained variance
406 of each EOF of the two periods. This change in the relative amount of variance represented by the individual EOFs may
407 indicate changes in the spatial structure of precipitation variability between the ERP and PI periods.



408
409 **Figure 9: Patterns of the first three non-rotated EOFs of winter (DJF) precipitation for PI (1800-1850 CE; a, b, c) and ERP**
410 **(400-362 BCE; d, e, f) and total explained variance for each EOF.**

411 In Figure 10, the regression maps (i.e., the regression coefficients $\beta_1(j, k)$ according to Eq. (3)) are shown, between the
412 three precipitation principal components ($PC(j)$) and the SLP fields from the driving MPI-ESM-P “Mythos” for the same
413 periods. All regression maps show very similar spatial patterns, albeit with varying amplitudes between the two periods.
414 This change in the amplitude of the regression coefficients may indicate variations in the robustness and strength of the
415 underlying relationships between the precipitation PCs and the large-scale SLP fields.

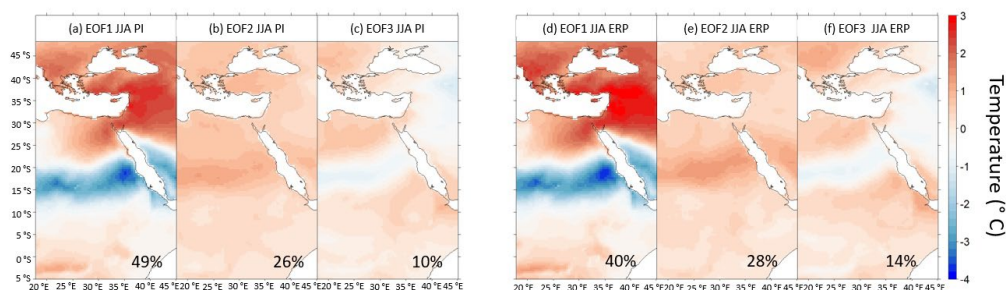
416 The EOF1 positive winter precipitation anomalies along the western coasts of the peninsulas of EM (Fig. 9a, d) are
417 connected with lower pressure over the Mediterranean (Fig. 10a, d) which is related to the higher frequency of cyclones
418 from the Gulf of Genoa or of Atlantic origin moving eastward, which, together with the orographic lifting, lead to high
419 amounts of precipitation over these areas. The dipole structure of winter precipitation EOF2 (Fig. 9b, e) with drier
420 conditions over western EM and wetter winters over its eastern part is linked to a statistically significant SLP dipole (or
421 tripole for ERP, Fig. 10b, e) with stable anomalous anticyclonic conditions (SLP positive anomalies) over the Eastern
422 Atlantic and western Europe and an anomalous trough with negative SLP anomalies over the east. The dry conditions
423 over the eastern coasts of the Black Sea in EOF3 (Fig. 9c, f) are connected with the prevailing anomalous high pressure
424 centered north of the Caspian Sea and extended over Eurasia (Fig. 10c, f). The ERP and PI periods represent a similar set
425 of regression patterns with different intensity for winter with respect to the influence of large-scale circulation.



426

427 **Figure 10: Regression maps between the PCs of the first three non-rotated winter (DJF) precipitation and SLP from the Mythos**
428 **simulation for the PI (a, b, c) and ERP (d, e, f) periods. Statistical significance at the 95 % confidence level is denoted with**
429 **dotted areas.**

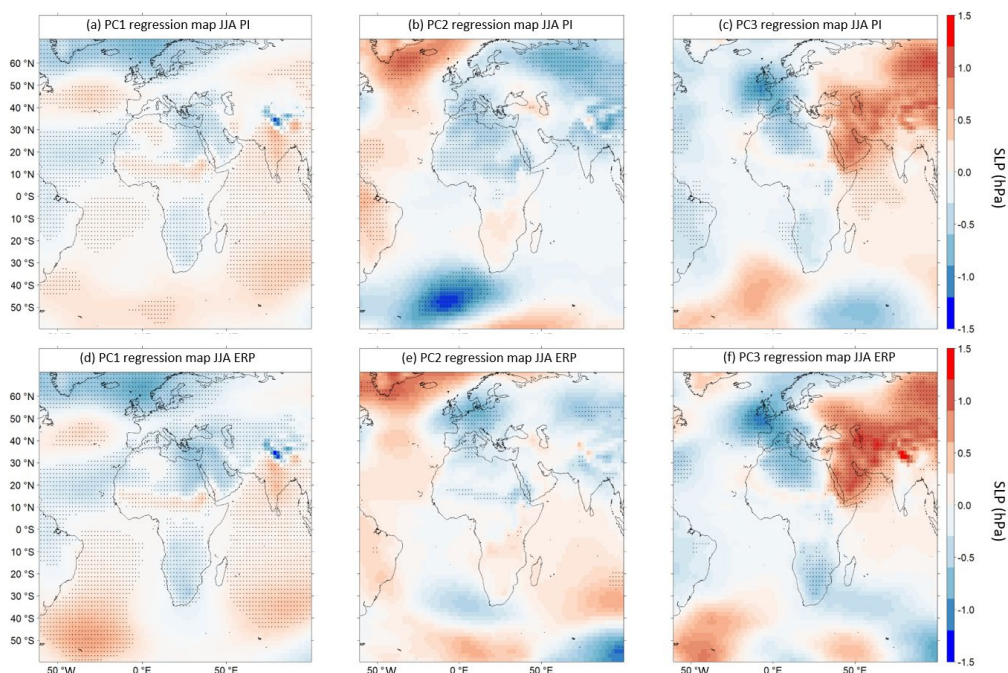
430 Figure 11 shows the leading three EOF patterns for summer 2m air temperatures over the EMNR region during the PI (a,
431 b, c) and ERP (d, e, f) periods that together represent nearly 85% of the total variance. Notably, the first EOF of the PI
432 period explains nearly half of the variance, while the ERP period exhibits a lower but still high contribution of 40%. The
433 EOF patterns show a high degree of similarity between the PI and ERP periods. The EOF1, as depicted in Figure 11 (a
434 and d), shows a clear temperature dipole pattern, characterized by distinctive negative temperature anomalies over the
435 African Sahel region (likely associated with ITCZ-related variability) and pronounced positive temperature anomalies
436 over EM, extending to the Middle East and Egypt. This dipole structure indicates the presence of an apparent
437 teleconnection between the Mediterranean Sea /Northern Africa and the Sahel region, resembling a temperature sea-saw
438 pattern. The second EOF air temperature patterns (Fig. 11b, e) for the PI and ERP periods show positive anomalies
439 throughout the entire EMNR area, while an intensified positive temperature anomalies signal is shown between 10 to 20
440 degrees north (Sahel). This pattern indicates similar variations of the two periods over the entire region that are
441 uncorrelated to the temperature sea-saw depicted in EOF1. The EOF3 (Fig. 11c, f) shows weak negative temperature
442 anomalies over the African Sahel region shifted slightly to the north, compared to EOF1, with negative anomalies
443 extending over the Middle East and weak positive anomalies over the Balkans. This pattern shows lower values in the
444 amount of explained variance.



445

446 **Figure 11: Patterns of the first three non-rotated EOFs of summer (JJA) temperature for PI (1800-1850 CE; a, b, c) and ERP**
447 **(400-362 BCE; d, e, f) and total explained variance for each EOF.**

448 The strong positive temperature anomalies over the northern and eastern part of the area and the belt of negative anomalies
449 over the subtropical region in EOF1 is reflected in the SLP regression map (Fig. 12a, d). The EOF1 temperature pattern
450 is related to negative SLP anomalies over the northern North Atlantic and positive anomalies over the central North
451 Atlantic, potentially connected with an intensified subtropical anticyclone, as well as negative anomalies over the
452 extended study area, which may indicate the influence of the Persian trough extend from the Asian Monsoon trough
453 (Lelieveld et al., 2012). Positive SLP anomalies are located over the belt of negative anomalies over the subtropical
454 region. The EOF2 positive temperature anomalies over the entire EMNR area are connected to negative SLP anomalies
455 over the region (Fig 12b, e). The higher temperatures over the area may be connected with an intensified Sahara heat low,
456 which is an area of low surface pressure as a response high low-level temperatures (Lavaysse et al., 2009; Messenger et
457 al., 2010). The third EOF of the two periods (Fig. 11c, f) explains a smaller amount of variance and thus the interpretation
458 of the patterns and the corresponding regression maps (Fig. 12c, f) is challenging and here not attempted.
459



460

461 **Figure 12: Regression maps between the PCs of the first three non-rotated summer (JJA) temperature and SLP from the**
462 **Mythos simulation for the PI (a, b, c) and ERP (d, e, f) periods. Statistical significance at the 95 % confidence level is denoted**
463 **with dotted areas.**

464 4 Conclusions

465 In this study, we presented the first fully forced CCLM adapted for paleoclimatic applications including volcanic, solar,
466 land-use, greenhouse gases, and orbital forcings with a spatial resolution of 0.44° over the extended area of the Eastern
467 Mediterranean and the Nile River Basin. We evaluated the performance of the model in the present time (1980-2018) and
468 compared the simulated climate for Early Roman Period, ERP (400-362 BCE) and the pre-industrial, PI (1800-1850 CE)
469 period.

470 Our study demonstrates that the fully forced paleo CCLM can simulate reasonably the climate within the selected region.
471 In general, the model exhibits better performance in simulating the seasonal air temperature compared to precipitation.
472 Especially within the Nile River domain, the simulated precipitation is less accurate, possibly due to the model's
473 limitations in representing convective processes linked to the ITCZ. Another important factor relates to the sparse network
474 of observational data over those areas, further complicating a proper comparison between simulated and observed
475 precipitation. In contrast, the model performs better in capturing precipitation patterns over the eastern Mediterranean.
476 The drying bias that occurs in the EM (especially in summer) may be related to the model's underestimation of total cloud
477 cover. Moreover, the model tends to underestimate temperatures in northern Africa (around 10° - 32° N) during winter
478 and the Sahel (10° - 20° N) during summer. During summer, temperatures in North Africa and the EM are showing a
479 warm bias.

480 In terms of the annual cycle of precipitation and temperature, the average climatic conditions were comparable between
481 the two periods, but the climatic variability varied across the study area. The ERP over the EM was generally wetter than



482 the PI in both summer and winter, with greater variability in summer. In the NR region, there were no statistically
 483 significant differences during the ERP winter compared to the PI, while summers during the ERP were predominantly
 484 wetter and reflected a larger variability compared to the PI period. However, we have found that the CCLM has limitations
 485 in capturing a realistic rainfall pattern over the NR region.

486 The links between the regional precipitation and temperature patterns and large-scale features were investigated using a
 487 linear regression approach between the principal components of summer temperature and winter precipitation onto the
 488 sea level pressure. The according results indicate consistent associations between precipitation/temperature EOF patterns
 489 and corresponding SLP anomalies during both periods. The major winter precipitation patterns over EM shown in the
 490 principle component analysis are found to be related to the cyclones/anticyclones of the surrounding area (such as the
 491 Eastern Atlantic, the Western Europe) together with the orographical lifting. While, the NR region is located under the
 492 ITCZ and is subject to various circulation mechanisms, which poses a challenge for the model to accurately simulate the
 493 local climate and its variability.

494 Future studies may involve adjusting physical parameters such as albedo, soil layers and aerosols to improve the
 495 performance of COSMO-CLM in capturing precipitation patterns in the NR region. Detailed investigations of the linkages
 496 between temperature and specific large-scale circulations in the EMNR region are also needed to provide a comprehensive
 497 understanding of the teleconnections in the study area. For paleoclimate research, comparing modeled data with proxy
 498 records is essential for a comprehensive understanding of climate variability and change over the past 2500 years and
 499 improvement of the climate models. Additionally, establishing connections between climate events and historically
 500 documented societal developments can provide insights into the role of climate change in the context of historical socio-
 501 economic changes.

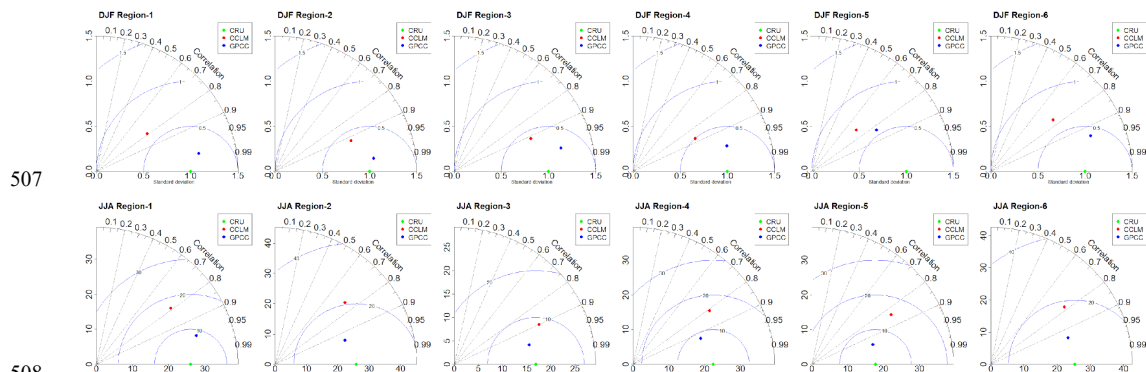
502 Appendix A

503 **Table A1: Spatial correlation of the CCLM and ERA with the first six CRU temperature REOFs for winter (DJF) and summer**
 504 **(JJA) over the EMNR. All values are significant at the 95% significance level. Numbers in parentheses give the corresponding**
 505 **REOFs of each data set.**

Winter (December, January, February)						
$r_{\text{CRU-CCLM}}$	0.79 (1 & 1)	0.78 (2 & 2)	0.88 (3 & 5)	0.93 (4 & 3)	0.73 (5 & 10)	0.57 (6 & 2)
$r_{\text{CRU-ERA}}$	0.93 (1 & 1)	0.93 (2 & 2)	0.93 (3 & 5)	0.94 (4 & 3)	0.84 (5 & 4)	0.85 (6 & 10)
Summer (June, July, August)						
$r_{\text{CRU-CCLM}}$	-0.76 (1 & 1)	0.69 (2 & 1)	0.73 (3 & 3)	0.51 (4 & 9)	0.86 (5 & 6)	0.75 (6 & 2)
$r_{\text{CRU-ERA}}$	-0.77 (1 & 1)	0.64 (2 & 2)	0.78 (3 & 3)	0.83 (4 & 2)	0.90 (5 & 6)	0.67 (6 & 4)

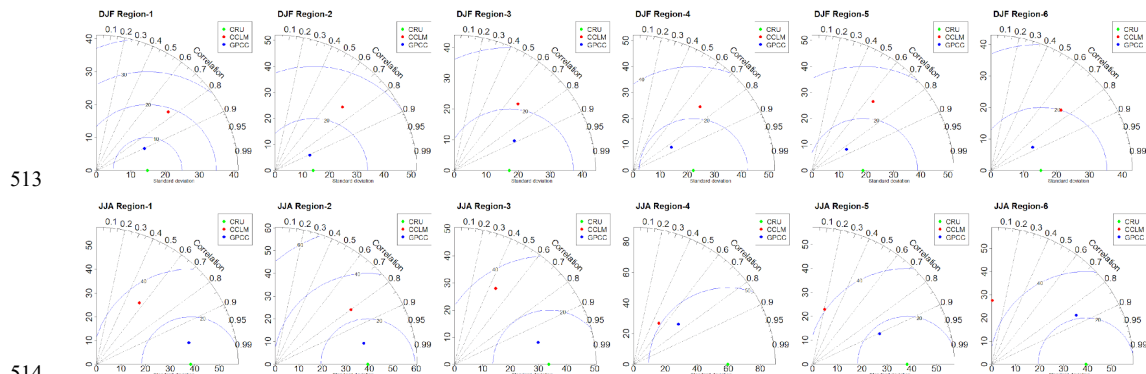


506 Appendix B



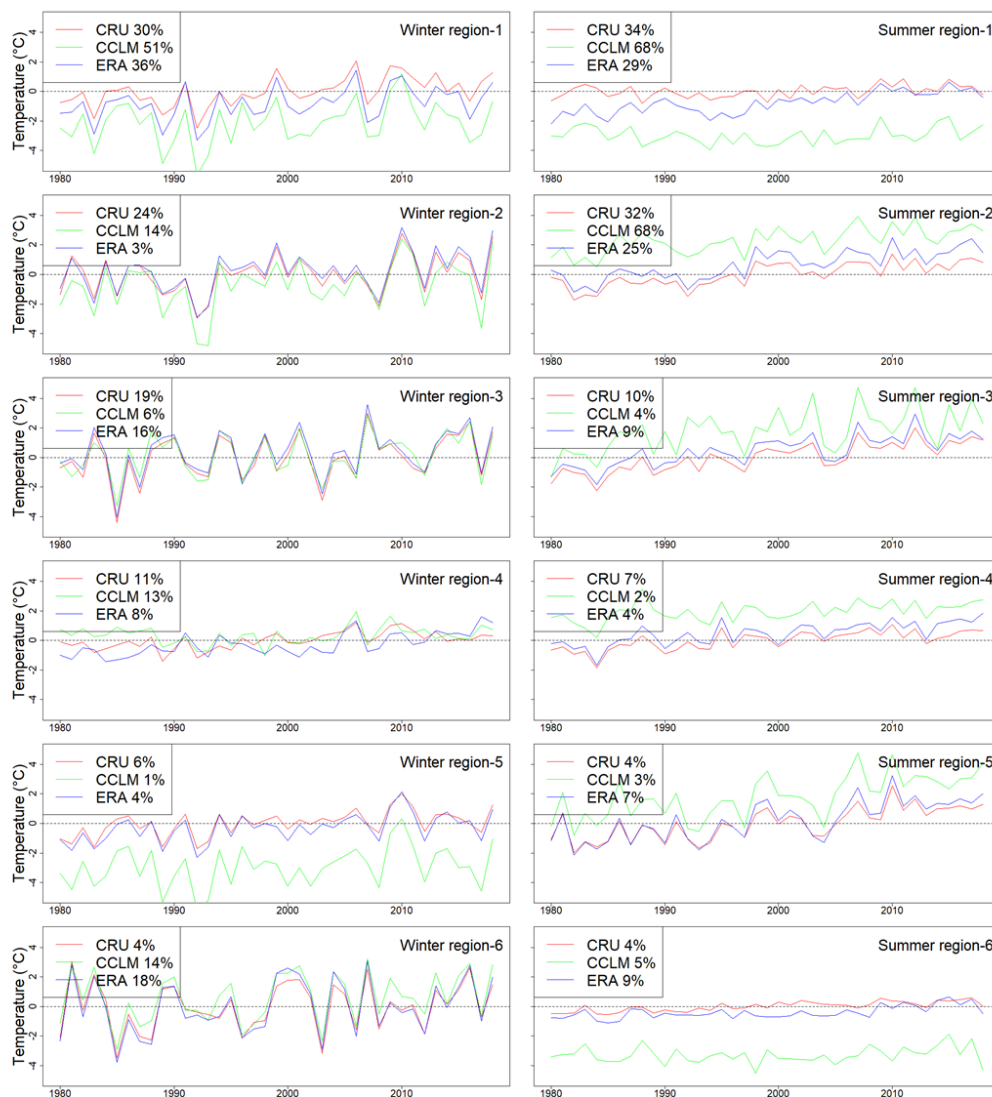
508
509 **Figure B1:** Taylor diagrams of winter (DJF) and summer (JJA) precipitation differences with respect to the CRU data set for
510 the period 1980 – 2018 for the Eastern Mediterranean regions. The green dot indicated CRU data set, therefore the correlations
511 showing in the plot is 1, and the blue (red) dot indicate the correlations between CCLM (GPCC) with CRU data sets.

512



514
515 **Figure B2:** Taylor diagrams of winter (DJF) and summer (JJA) precipitation differences with respect to the CRU data set for
516 the period 1980 – 2018 for the Nile River Basin regions. The green dot indicated CRU data set, therefore the correlations
517 showing in the plot is 1, and the blue (red) dot indicate the correlations between CCLM (GPCC) with CRU data sets.

518



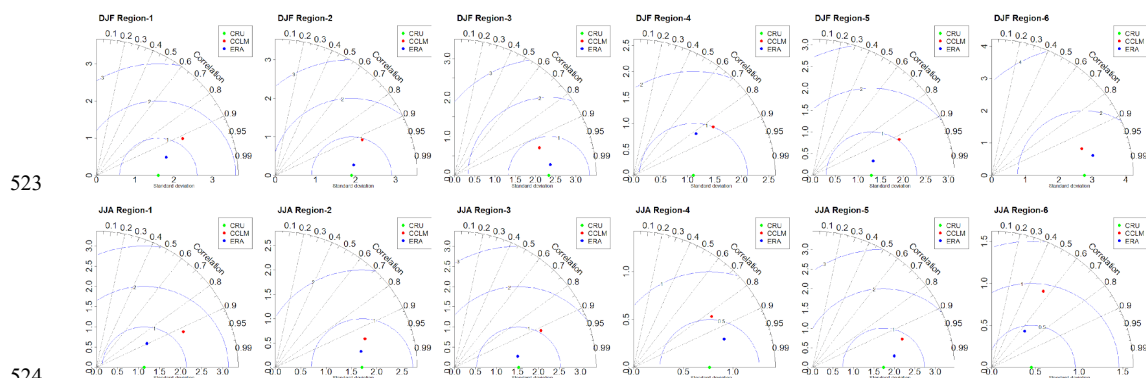
519

520

521

Figure B3: Seasonal mean total temperature differences of EMNR regions with respect to the 1980-2018 mean total CRU winter (DJF) and summer (JJA) temperature.

522



523
524 **Figure B4:** Taylor diagrams of winter (DJF) and summer (JJA) precipitation differences with respect to the CRU data set for
525 the period 1980 – 2018 for the Eastern Mediterranean/Nile River Basin regions. The green dot indicated CRU data set, therefore
526 the correlations showing in the plot is 1, and the blue (red) dot indicate the correlations between CCLM (ERA-Interim) with
527 CRU data sets.
528

529 **Code availability**

530 The COSMO-CLM model is available and free of charge for all members of the CLM-Community via their website
531 <https://www.clmcommunity.eu/>. The user must either be a member of the CLM-Community or the respective institute
532 must possess an institutional license. The changes in the original source code for implementing the external forcings are
533 described in detail in Hartmann et al., (submitted).

534 **Data availability**

535 The simulated data by COSMO-CLM in this paper is stored at the Deutsches Klimarechenzentrum (DKRZ).

536 **Competing interests**

537 The authors declare that they have no conflict of interest.

538 **Author contribution**

539 MZ and EH developed the model code and performed the simulations. EX, SW, MA and MZ contributed to the
540 conceptualization of the manuscript. MZ conducted the formal analysis with the support of SW and NL. MZ prepared the
541 manuscript. All authors followed the analysis from the beginning, provided text and edited/commented the final version
542 of the manuscript.

543 **Acknowledgement**

544 This work used resources of the Deutsches Klimarechenzentrum (DKRZ) granted by its Scientific Steering Committee
545 (WLA) under project number bb1201. EX acknowledges support by the Greek “National Research Network on Climate
546 Change and its Impact” (project code 200/937). EX, NL acknowledge support by the EU Horizon 2020 Project CLINT



547 under Grant Agreement number 101003876. EX, MA acknowledge support by the German Federal Ministry of Education
548 and Research (BMBF) project NUKLEUS (grant number 01LR2002F).

549 **References**

550 Adam, O., Schneider, T., Brient, F., and Bischoff, T.: Relation of the double-ITCZ bias to the atmospheric energy budget
551 in climate models, *Geophysical Research Letters*, 43, 7670–7677, <https://doi.org/10.1002/2016GL069465>, 2016.

552 Alemseged, T. H. and Tom, R.: Evaluation of regional climate model simulations of rainfall over the Upper Blue Nile
553 basin, *Atmospheric Research*, 161–162, 57–64, <https://doi.org/10.1016/j.atmosres.2015.03.013>, 2015.

554 Alpert, P., Price, C., Krichak, S. O., Ziv, B., Saaroni, H., Osetinsky, I., Barkan, J., and Kishcha, P.: Tropical tele-
555 connections to the Mediterranean climate and weather, *Advances in Geosciences*, 2, 157–160,
556 <https://doi.org/10.5194/adgeo-2-157-2005>, 2005.

557 Armstrong, E., Hopcroft, P. O., and Valdes, P. J.: Reassessing the Value of Regional Climate Modeling Using
558 Paleoclimate Simulations, *Geophysical Research Letters*, 46, 12464–12475, <https://doi.org/10.1029/2019GL085127>,
559 2019.

560 Bader, J., Jungclaus, J., Krivova, N., Lorenz, S., Maycock, A., Raddatz, T., Schmidt, H., Toohey, M., Wu, C.-J., and
561 Claussen, M.: Global temperature modes shed light on the Holocene temperature conundrum, *Nature Communications*,
562 11, <https://doi.org/10.1038/s41467-020-18478-6>, 2020.

563 Berger, A.: Long-Term Variations of Daily Insolation and Quaternary Climatic Changes, *American Meteorological*
564 *Society*, 1978.

565 Bray, D. and Von Storch, H.: The Bray and von Storch 5th International Survey of Climate Scientists 2015/2016,
566 <https://doi.org/10.13140/RG.2.2.11802.85443>, 2016.

567 Bucchignani, E., Cattaneo, L., Panitz, H.-J., and Mercogliano, P.: Sensitivity analysis with the regional climate model
568 COSMO-CLM over the CORDEX-MENA domain, *Meteorology and Atmospheric Physics*, 128, 73–95,
569 <https://doi.org/10.1007/s00703-015-0403-3>, 2016.

570 Camberlin, P.: Nile basin climates, in: *The Nile*, Springer, 307–333, 2009.

571 Conway, D.: The climate and hydrology of the Upper Blue Nile River, *Geographical Journal*, 166, 49–62, 2000.

572 Cramer, W., Guiot, J., Fader, M., Garrabou, J., Gattuso, J.-P., Iglesias, A., Lange, M. A., Lionello, P., Llasat, M. C., Paz,
573 S., Peñuelas, J., Snoussi, M., Toreti, A., Tsimplis, M. N., and Xoplaki, E.: Climate change and interconnected risks to
574 sustainable development in the Mediterranean, *Nature Clim Change*, 8, 972–980, <https://doi.org/10.1038/s41558-018-0299-2>,
575 2018.

576 Crowley, T., GA, Z., Vinther, B., Udisti, R., Kreutz, K., Cole-Dai, J., and Castellano, E.: Volcanism and the Little Ice
577 Age, *PAGES Newsl.*, 16, 22–23, <https://doi.org/10.1029/2002GL0166335>, 2008.

578 Cubasch, U., Zorita, E., Kaspar, F., Gonzalez-Rouco, J. F., Storch, H. von, and Prömmel, K.: Simulation of the role of
579 solar and orbital forcing on climate, *Advances in Space Research*, 37, 1629–1634,
580 <https://doi.org/10.1016/j.asr.2005.04.076>, 2006.

581 Dee, D. P., Uppala, S. M., Simmons, A. J., Berrisford, P., Poli, P., Kobayashi, S., Andrae, U., Balmaseda, M. A., Balsamo,
582 G., Bauer, P., Bechtold, P., Beljaars, A. C. M., van de Berg, L., Bidlot, J., Bormann, N., Delsol, C., Dragani, R., Fuentes,
583 M., Geer, A. J., Haimberger, L., Healy, S. B., Hersbach, H., Hólm, E. V., Isaksen, I., Kållberg, P., Köhler, M., Matricardi,
584 M., McNally, A. P., Monge-Sanz, B. M., Morcrette, J.-J., Park, B.-K., Peubey, C., de Rosnay, P., Tavalato, C., Thépaut,
585 J.-N., and Vitart, F.: The ERA-Interim reanalysis: configuration and performance of the data assimilation system,
586 *Quarterly Journal of the Royal Meteorological Society*, 137, 553–597, <https://doi.org/10.1002/qj.828>, 2011.



- 587 Dieng, D., Smiatek, G., Heinzeller, D., and Kunstmann, H.: Simulation of the Rain Belt of the West African Monsoon
588 (WAM) in High Resolution CCLM Simulation, in: High Performance Computing in Science and Engineering '16, Cham,
589 547–558, https://doi.org/10.1007/978-3-319-47066-5_37, 2016.
- 590 Doms, G., Forstner, J., Heise, E., Reinhardt, T., Ritter, B., and Schrodin, R.: A Description of the Nonhydrostatic Regional
591 COSMO Model, 161, 2011.
- 592 Gallacher, K., Miller, C., Scott, E. M., Willows, R., Pope, L., and Douglass, J.: Flow-directed PCA for monitoring
593 networks, *Environmetrics*, 28, e2434, <https://doi.org/10.1002/env.2434>, 2017.
- 594 García-Herrera, R., Luterbacher, J., Lionello, P., González-Rouco, F., Ribera, P., Rodó, X., Kull, C., and Zerefos, C.:
595 Reconstruction of past Mediterranean climate, *Eos, Transactions American Geophysical Union*, 88, 111–111,
596 <https://doi.org/10.1029/2007EO090010>, 2007.
- 597 Giorgi, F.: Thirty Years of Regional Climate Modeling: Where Are We and Where Are We Going next?, *Journal of*
598 *Geophysical Research: Atmospheres*, 124, 5696–5723, <https://doi.org/10.1029/2018JD030094>, 2019.
- 599 Gómez-Navarro, J. J. and Zorita, E.: Atmospheric annular modes in simulations over the past millennium: No long-term
600 response to external forcing, *Geophysical Research Letters*, 40, 3232–3236, <https://doi.org/10.1002/grl.50628>, 2013.
- 601 Gomez-Navarro, J. J., Wagner, S., Zorita, E., and Montavez, J. P.: Changes in distribution of daily temperature and
602 precipitation between the Late Maunder Minimum and the 2nd half of the 20th century: A regional model study, 2012,
603 PP21B-1990, 2012.
- 604 Gray, L. J., Beer, J., Geller, M., Haigh, J. D., Lockwood, M., Matthes, K., Cubasch, U., Fleitmann, D., Harrison, G.,
605 Hood, L., Luterbacher, J., Meehl, G. A., Shindell, D., van Geel, B., and White, W.: Solar Influences on Climate, *Reviews*
606 *of Geophysics*, 48, <https://doi.org/10.1029/2009RG000282>, 2010.
- 607 Haldon, J., Roberts, N., Izdebski, A., Fleitmann, D., McCormick, M., Cassis, M., Doonan, O., Eastwood, W., Elton, H.,
608 Ladstätter, S., Manning, S., Newhard, J., Nicoll, K., Telelis, I., and Xoplaki, E.: The Climate and Environment of
609 Byzantine Anatolia: Integrating Science, History, and Archaeology, *The Journal of Interdisciplinary History*, 45, 113–
610 161, https://doi.org/10.1162/JINH_a_00682, 2014.
- 611 Haldon, J., Mordechai, L., Newfield, T. P., Chase, A. F., Izdebski, A., Guzowski, P., Labuhn, I., and Roberts, N.: History
612 meets palaeoscience: Consilience and collaboration in studying past societal responses to environmental change,
613 *Proceedings of the National Academy of Sciences*, 115, 3210–3218, <https://doi.org/10.1073/pnas.1716912115>, 2018.
- 614 Harris, I., Osborn, T. J., Jones, P., and Lister, D.: Version 4 of the CRU TS monthly high-resolution gridded multivariate
615 climate dataset, *Sci Data*, 7, 109, <https://doi.org/10.1038/s41597-020-0453-3>, 2020.
- 616 Hartmann, E., Zhang, M., Xoplaki, E., Wagner, S., and Adakudlu, M.: Implementing External Climate Forcings into the
617 COSMO-CLM - A Sensitivity Study around the Decade of the Samalas Volcanic Eruption in the EMME region,
618 *Geoscientific Model Development*, submitted.
- 619 Hennessy, K., Lawrence, J., and Mackey, B.: IPCC Sixth Assessment Report (AR6): Climate Change 2022 - Impacts,
620 *Adaptation and Vulnerability: Regional Factsheet Australasia*, 2022.
- 621 Hochman, A., Marra, F., Messori, G., Pinto, J. G., Raveh-Rubin, S., Yosef, Y., and Zittis, G.: Extreme weather and
622 societal impacts in the eastern Mediterranean, *Earth System Dynamics*, 13, 749–777, [https://doi.org/10.5194/esd-13-749-](https://doi.org/10.5194/esd-13-749-2022)
623 2022, 2022.
- 624 Jameson, A., Schmidt, W., and Turkel, E.: Numerical solution of the Euler equations by finite volume methods using
625 Runge Kutta time stepping schemes, in: 14th Fluid and Plasma Dynamics Conference, American Institute of Aeronautics
626 and Astronautics, <https://doi.org/10.2514/6.1981-1259>, 1981.
- 627 Jungclaus, J. H., Bard, E., Baroni, M., Braconnot, P., Cao, J., Chini, L. P., Egorova, T., Evans, M., González-Rouco, J.
628 F., Goosse, H., Hurtt, G. C., Joos, F., Kaplan, J. O., Khodri, M., Klein Goldewijk, K., Krivova, N., LeGrande, A. N.,
629 Lorenz, S. J., Luterbacher, J., Man, W., Maycock, A. C., Meinshausen, M., Moberg, A., Muscheler, R., Nehrbaas-Ahles,
630 C., Otto-Bliessner, B. I., Phipps, S. J., Pongratz, J., Rozanov, E., Schmidt, G. A., Schmidt, H., Schmutz, W., Schurer, A.,
631 Shapiro, A. I., Sigl, M., Smerdon, J. E., Solanki, S. K., Timmreck, C., Toohey, M., Usoskin, I. G., Wagner, S., Wu, C.-



- 632 J., Yeo, K. L., Zanchettin, D., Zhang, Q., and Zorita, E.: The PMIP4 contribution to CMIP6 – Part 3: The last millennium,
633 scientific objective, and experimental design for the PMIP4 *past1000* simulations, *Geoscientific Model Development*, 10,
634 4005–4033, <https://doi.org/10.5194/gmd-10-4005-2017>, 2017.
- 635 Kageyama, M., Braconnot, P., Harrison, S. P., Haywood, A. M., Jungclaus, J. H., Otto-Bliesner, B. L., Peterschmitt, J.-
636 Y., Abe-Ouchi, A., Albani, S., Bartlein, P. J., Brierley, C., Crucifix, M., Dolan, A., Fernandez-Donado, L., Fischer, H.,
637 Hopcroft, P. O., Ivanovic, R. F., Lambert, F., Lunt, D. J., Mahowald, N. M., Peltier, W. R., Phipps, S. J., Roche, D. M.,
638 Schmidt, G. A., Tarasov, L., Valdes, P. J., Zhang, Q., and Zhou, T.: The PMIP4 contribution to CMIP6 – Part 1: Overview
639 and over-arching analysis plan, *Geoscientific Model Development*, 11, 1033–1057, <https://doi.org/10.5194/gmd-11-1033-2018>, 2018.
- 641 Kelley, C. P., Mohtadi, S., Cane, M. A., Seager, R., and Kushnir, Y.: Climate change in the Fertile Crescent and
642 implications of the recent Syrian drought, *Proceedings of the National Academy of Sciences*, 112, 3241–3246,
643 <https://doi.org/10.1073/pnas.1421533112>, 2015.
- 644 Lange, M. A., Llasat, M. C., Snoussi, M., Graves, A., Tellier, J. L., Queralt, A., and Vagliasindi, G. M.: First
645 Mediterranean Assessment Report – Chapter 1: Introduction, Zenodo, <https://doi.org/10.5281/zenodo.7100592>, 2020.
- 646 Lavaysse, C., Flamant, C., Janicot, S., Parker, D. J., Lafore, J.-P., Sultan, B., and Pelon, J.: Seasonal evolution of the West
647 African heat low: a climatological perspective, *Clim Dyn*, 33, 313–330, <https://doi.org/10.1007/s00382-009-0553-4>,
648 2009.
- 649 Lelieveld, J., Hadjinicolaou, P., Kostopoulou, E., Chenoweth, J., El Maayar, M., Giannakopoulos, C., Hannides, C.,
650 Lange, M. A., Tanarhte, M., Tyrllis, E., and Xoplaki, E.: Climate change and impacts in the Eastern Mediterranean and
651 the Middle East, *Climatic Change*, 114, 667–687, <https://doi.org/10.1007/s10584-012-0418-4>, 2012.
- 652 Ludwig, P., Schaffernicht, E., Shao, Y., and Pinto, J.: Regional atmospheric circulation over Europe during the Last
653 Glacial Maximum and its links to precipitation, *Journal of Geophysical Research Atmospheres*, 121, 2130–2145,
654 <https://doi.org/10.1002/2015JD024444>, 2016.
- 655 Ludwig, P., Pinto, J., Raible, C., and Shao, Y.: Impacts of Surface Boundary Conditions on Regional Climate Model
656 Simulations of European Climate during the Last Glacial Maximum, *Geophysical Research Letters*, 44, 5086–5095,
657 <https://doi.org/10.1002/2017GL073622>, 2017.
- 658 Luterbacher, J. and Pfister, C.: The year without a summer, *Nature Geosci*, 8, 246–248, <https://doi.org/10.1038/ngeo2404>,
659 2015.
- 660 Luterbacher, J., Werner, J. P., Smerdon, J. E., Fernández-Donado, L., González-Rouco, F. J., Barriopedro, D., Ljungqvist,
661 F. C., Büntgen, U., Zorita, E., Wagner, S., Esper, J., McCarroll, D., Toreti, A., Frank, D., Jungclaus, J. H., Barriendos,
662 M., Bertolin, C., Bothe, O., Brázdil, R., Camuffo, D., Dobrovolný, P., Gagen, M., García-Bustamante, E., Ge, Q., Gómez-
663 Navarro, J. J., Guiot, J., Hao, Z., Hegerl, G. C., Holmgren, K., Klimenko, V. V., Martín-Chivelet, J., Pfister, C., Roberts,
664 N., Schindler, A., Schurer, A., Solomina, O., Gunten, L. von, Wahl, E., Wanner, H., Wetter, O., Xoplaki, E., Yuan, N.,
665 Zanchettin, D., Zhang, H., and Zerefos, C.: European summer temperatures since Roman times, *Environ. Res. Lett.*, 11,
666 024001, <https://doi.org/10.1088/1748-9326/11/2/024001>, 2016.
- 667 Manning, J. G., Ludlow, F., Stine, A. R., Boos, W. R., Sigl, M., and Marlon, J. R.: Volcanic suppression of Nile summer
668 flooding triggers revolt and constrains interstate conflict in ancient Egypt, *Nat Commun*, 8, 900,
669 <https://doi.org/10.1038/s41467-017-00957-y>, 2017.
- 670 Meinshausen, M., Vogel, E., Nauels, A., Lorbacher, K., Meinshausen, N., Etheridge, D. M., Fraser, P. J., Montzka, S. A.,
671 Rayner, P. J., Trudinger, C. M., Krummel, P. B., Beyerle, U., Canadell, J. G., Daniel, J. S., Enting, I. G., Law, R. M.,
672 Lunder, C. R., O’Doherty, S., Prinn, R. G., Reimann, S., Rubino, M., Velders, G. J. M., Vollmer, M. K., Wang, R. H. J.,
673 and Weiss, R.: Historical greenhouse gas concentrations for climate modelling (CMIP6), *Geoscientific Model
674 Development*, 10, 2057–2116, <https://doi.org/10.5194/gmd-10-2057-2017>, 2017.
- 675 Ménot, G., Pivot, S., Bouloubassi, I., Davtian, N., Hennekam, R., Bosch, D., Ducassou, E., Bard, E., Migeon, S., and
676 Revel, M.: Timing and stepwise transitions of the African Humid Period from geochemical proxies in the Nile deep-sea
677 fan sediments, *Quaternary Science Reviews*, 228, 106071, <https://doi.org/10.1016/j.quascirev.2019.106071>, 2020.



- 678 Messenger, C., Parker, D. J., Reitebuch, O., Agusti-Panareda, A., Taylor, C. M., and Cuesta, J.: Structure and dynamics of
679 the Saharan atmospheric boundary layer during the West African monsoon onset: observations and analyses from the
680 research flights of 14 and 17 July 2006, *Quarterly Journal of the Royal Meteorological Society*, 136, 107–124,
681 <https://doi.org/10.1002/qj.469>, 2010.
- 682 Nicholson, S. E.: The ITCZ and the Seasonal Cycle over Equatorial Africa, *Bulletin of the American Meteorological*
683 *Society*, 99, 337–348, <https://doi.org/10.1175/BAMS-D-16-0287.1>, 2018.
- 684 Paz, S., Tourre, Y. M., and Planton, S.: North Africa-West Asia (NAWA) sea-level pressure patterns and their linkages
685 with the Eastern Mediterranean (EM) climate, *Geophysical Research Letters*, 30, <https://doi.org/10.1029/2003GL017862>,
686 2003.
- 687 Pielke Sr, R., Pitman, A., Niyogi, D., Mahmood, R., Mcalpine, C., Hossain, F., Klein Goldewijk, K., Nair, U., Betts, R.,
688 Fall, S., Reichstein, M., Kabat, P., and de NOBLET, N.: Land Use/Land Cover Changes and Climate: Modeling Analysis
689 and Observational Evidence, *Wiley Interdisciplinary Reviews: Climate Change*, 2, 828–850,
690 <https://doi.org/10.1002/wcc.144>, 2011.
- 691 Pörtner, H.-O., Roberts, D. C., Tignor, M. M. B., Poloczanska, E. S., Mintenbeck, K., Alegría, A., Craig, M., Langsdorf,
692 S., Löschke, S., Möller, V., Okem, A., and Rama, B. (Eds.): *Climate Change 2022: Impacts, Adaptation and Vulnerability.*
693 *Contribution of Working Group II to the Sixth Assessment Report of the Intergovernmental Panel on Climate Change.*,
694 2022.
- 695 Raffa, M., Adinolfi, M., Reder, A., Marras, G. F., Mancini, M., Scipione, G., Santini, M., and Mercogliano, P.: Very High
696 Resolution Projections over Italy under different CMIP5 IPCC scenarios, *Sci Data*, 10, 238,
697 <https://doi.org/10.1038/s41597-023-02144-9>, 2023.
- 698 Ramanathan, V. and Feng, Y.: Air pollution, greenhouse gases and climate change: Global and regional perspectives,
699 *Atmospheric Environment*, 43, 37–50, <https://doi.org/10.1016/j.atmosenv.2008.09.063>, 2009.
- 700 Renssen, H., Isarin, R. F. B., Jacob, D., Podzun, R., and Vandenberghe, J.: Simulation of the Younger Dryas climate in
701 Europe using a regional climate model nested in an AGCM: preliminary results, *Global and Planetary Change*, 30, 41–
702 57, [https://doi.org/10.1016/S0921-8181\(01\)00076-5](https://doi.org/10.1016/S0921-8181(01)00076-5), 2001.
- 703 Robock, A.: Volcanic eruptions and climate, *Reviews of Geophysics*, 38, 191–219,
704 <https://doi.org/10.1029/1998RG000054>, 2000.
- 705 Rockel, B., Will, A., and Hense, A.: Regional climate modelling with COSMO-CLM (CCLM), *Meteorol. Z. (Stuttg.)*, 17,
706 2008.
- 707 Schättler, U. and Blahak, U.: in: *A Description of the Nonhydrostatic Regional COSMO-Model*, 2017.
- 708 Schneider, U., Finger P, Rustemeier E, Ziese M, and Hänsel S: *Global Precipitation Analysis Products of the GPCP*,
709 2022.
- 710 Schulz, J.-P., Vogel, G., Becker, C., Kothe, S., Rummel, U., and Ahrens, B.: Evaluation of the ground heat flux simulated
711 by a multi-layer land surface scheme using high-quality observations at grass land and bare soil, *Meteorologische*
712 *Zeitschrift*, 25, 607–620, <https://doi.org/10.1127/metz/2016/0537>, 2016.
- 713 Singh, R., Tsigaridis, K., LeGrande, A. N., Ludlow, F., and Manning, J. G.: Investigating hydroclimatic impacts of the
714 168–158 BCE volcanic quartet and their relevance to the Nile River basin and Egyptian history, *Climate of the Past*, 19,
715 249–275, <https://doi.org/10.5194/cp-19-249-2023>, 2023.
- 716 Sørland, S. L., Brogli, R., Pothapakula, P. K., Russo, E., Van de Walle, J., Ahrens, B., Anders, I., Bucchignani, E., Davin,
717 E. L., Demory, M.-E., Dosio, A., Feldmann, H., Früh, B., Geyer, B., Keuler, K., Lee, D., Li, D., van Lipzig, N. P. M.,
718 Min, S.-K., Panitz, H.-J., Rockel, B., Schär, C., Steger, C., and Thiery, W.: COSMO-CLM regional climate simulations
719 in the Coordinated Regional Climate Downscaling Experiment (CORDEX) framework: a review, *Geoscientific Model*
720 *Development*, 14, 5125–5154, <https://doi.org/10.5194/gmd-14-5125-2021>, 2021.
- 721 Storch, H. V. and Zwiers, F. W.: *Statistical Analysis in Climate Research*, 1st ed., Cambridge University Press,
722 <https://doi.org/10.1017/CBO9780511612336>, 1984.



- 723 Tiedtke, M.: Parameterization of Cumulus Convection in Large-Scale Models, in: Physically-Based Modelling and
724 Simulation of Climate and Climatic Change, edited by: Schlesinger, M. E., Springer Netherlands, Dordrecht, 375–431,
725 https://doi.org/10.1007/978-94-009-3041-4_9, 1988.
- 726 Toohey, M. and Sigl, M.: Volcanic stratospheric sulfur injections and aerosol optical depth from 500 BCE to 1900 CE,
727 *Earth System Science Data*, 9, 809–831, <https://doi.org/10.5194/essd-9-809-2017>, 2017.
- 728 Viste, E. and Sorteberg, A.: Moisture transport into the Ethiopian highlands, *International Journal of Climatology*, 333,
729 249–263, <https://doi.org/10.1002/joc.3409>, 2013.
- 730 Wilks, D. S.: *Statistical Methods in the Atmospheric Sciences*, Academic Press, 698 pp., 2011.
- 731 Worku, G., Teferi, E., Bantider, A., Dile, Y. T., and Taye, M. T.: Evaluation of regional climate models performance in
732 simulating rainfall climatology of Jemma sub-basin, Upper Blue Nile Basin, Ethiopia, *Dynamics of Atmospheres and*
733 *Oceans*, 83, 53–63, <https://doi.org/10.1016/j.dynatmoce.2018.06.002>, 2018.
- 734 Xoplaki, E., Fleitmann, D., Luterbacher, J., Wagner, S., Haldon, J. F., Zorita, E., Telelis, I., Toreti, A., and Izdebski, A.:
735 The Medieval Climate Anomaly and Byzantium: A review of the evidence on climatic fluctuations, economic
736 performance and societal change, *Quaternary Science Reviews*, 136, 229–252,
737 <https://doi.org/10.1016/j.quascirev.2015.10.004>, 2016.
- 738 Xoplaki, E., Luterbacher, J., Wagner, S., Zorita, E., Fleitmann, D., Preiser-Kapeller, J., Sargent, A. M., White, S., Toreti,
739 A., Haldon, J. F., Mordechai, L., Bozkurt, D., Akçer-Ön, S., and Izdebski, A.: Modelling Climate and Societal Resilience
740 in the Eastern Mediterranean in the Last Millennium, *Hum Ecol*, 46, 363–379, [https://doi.org/10.1007/s10745-018-9995-](https://doi.org/10.1007/s10745-018-9995-9)
741 9, 2018.
- 742 Xoplaki, E., Luterbacher, J., Luther, N., Behr, L., Wagner, S., Jungclaus, J., Zorita, E., Toreti, A., Fleitmann, D., Izdebski,
743 A., and Bloomfield, K.: Hydrological Changes in Late Antiquity: Spatio-Temporal Characteristics and Socio-Economic
744 Impacts in the Eastern Mediterranean, in: *Climate Change and Ancient Societies in Europe and the Near East: Diversity*
745 *in Collapse and Resilience*, edited by: Erdkamp, P., Manning, J. G., and Verboven, K., Springer International Publishing,
746 Cham, 533–560, https://doi.org/10.1007/978-3-030-81103-7_18, 2021.
- 747 Zhang, M., Tölle, M. H., Hartmann, E., Xoplaki, E., and Luterbacher, J.: A Sensitivity Assessment of COSMO-CLM to
748 Different Land Cover Schemes in Convection-Permitting Climate Simulations over Europe, *Atmosphere*, 12, 1595,
749 <https://doi.org/10.3390/atmos12121595>, 2021.
- 750 Zittis, G., Almazroui, M., Alpert, P., Ciais, P., Cramer, W., Dahdal, Y., Fnais, M., Francis, D., Hadjinicolaou, P., Howari,
751 F., Jrrar, A., Kaskaoutis, D. G., Kulmala, M., Lazoglou, G., Mihalopoulos, N., Lin, X., Rudich, Y., Sciare, J., Stenchikov,
752 G., Xoplaki, E., and Lelieveld, J.: Climate Change and Weather Extremes in the Eastern Mediterranean and Middle East,
753 *Reviews of Geophysics*, 60, e2021RG000762, <https://doi.org/10.1029/2021RG000762>, 2022.

754